

Far-Infrared photometry of a statistical sample of late-type Virgo Cluster galaxies ¹

Richard J. Tuffs, Cristina C. Popescu^{2,3,4}, Daniele Pierini⁵, Heinrich J. Völk

Max Planck Institut für Kernphysik, Saupfercheckweg 1, 69117 Heidelberg, Germany

Hans Hippelein

Max Planck Institut für Astronomie, Königstuhl 17, 69117 Heidelberg, Germany

Kieron Leech, Leo Metcalfe

ISO Data Centre, Astrophysics Division, Space Science Department of ESA, Villafranca del Castillo, P.O. Box 50727, 28080 Madrid, Spain

Ingolf Heinrichsen and Cong Xu

IPAC(Caltech/JPL), 770 S. Wilson Avenue, Pasadena, California 91125, USA

ABSTRACT

We present deep diffraction-limited far-infrared (FIR) strip maps of a sample of 63 galaxies later than S0 and brighter than B_T 16.8, selected from the Virgo Cluster Catalogue of Binggeli, Sandage & Tammann (1985). The ISOPHOT instrument on board the Infrared Space Observatory was used to achieve sensitivities typically an order of magnitude deeper than IRAS in the 60 and 100 μm bands and to reach the confusion limit at 170 μm . The averaged 3σ upper limits for integrated flux densities of point sources at 60, 100 and 170 μm are 43, 33 and 58 mJy, respectively. 54 galaxies (85.7%) are detected at least at one wavelength, and 40 galaxies (63.5%) are detected at all three wavelengths. The highest detection rate (85.7%) is in the 170 μm band. In many cases the galaxies

²present address: The Observatories of the Carnegie Institution of Washington, 813 Santa Barbara Str., Pasadena, 91101 California, USA; email:popescu@ociw.edu

³Otto-Hahn Fellow of the Max Planck Institut für Astronomie, Königstuhl 17, 69117 Heidelberg, Germany

⁴Research Associate, The Astronomical Institute of the Romanian Academy, Str. Cuțitul de Argint 5, Bucharest, Romania

⁵present affiliation: The University of Toledo, Toledo, Ohio 43606-3390, USA

are resolved, allowing the scale length of the infrared disks to be derived from the oversampled brightness profiles in addition to the spatially integrated emission. The data presented should provide the basis for a variety of statistical investigations of the FIR spectral energy distributions of gas rich galaxies in the local universe spanning a broad range in star-formation activity and morphological types, including dwarf systems and galaxies with rather quiescent star formation activity.

Subject headings: catalogs—galaxies: clusters: individual (Virgo cluster)—galaxies: photometry—galaxies: statistics—infrared: galaxies—surveys

1. Introduction

Galaxy emission in the Far Infrared (FIR) is intimately connected to the current rate of star formation, since the characteristic radiation of young stars in the ultraviolet and optical wavelength range will at least in part be absorbed by interstellar dust. The IRAS all sky survey - within its limitations to wavelengths shorter than about $120\ \mu\text{m}$ - raised statistical studies of star formation in galaxies to a new level, detecting over 25,000 objects (see Soifer et al. 1987 for a review). Despite the bright (by optical standards) detection limit of ~ 0.5 and $1.5\ \text{Jy}$ at 60 and $100\ \mu\text{m}$, respectively, about half of the IRAS galaxies had no counterparts in optical catalogues at the time of the survey. In part, this was a consequence of the almost complete sky coverage and homogeneous data processing of the IRAS mission. However, it also reflected the fact that at luminosities greater than about $10^{11}\ L_{\odot}$ optically selected galaxies are less common than IRAS galaxies. These luminous infrared objects are thought to be relatively distant systems undergoing intense bursts of massive star formation, probably triggered by mergers and interactions, in which the bulk of the stellar luminosity is locally absorbed by dust and re-radiated in the FIR (see e.g. Sanders & Mirabel 1996 for a review, Leech et al. 1994).

In the local Universe the most common gas rich systems are the so-called “normal” late-type galaxies (later than S0). By “normal” we loosely refer to galaxies which are not dominated by an active nucleus and whose current star formation rates (SFRs) would be

¹Based on observations with ISO, an ESA project with instruments funded by ESA member states (especially the PI countries: France, Germany, the Netherlands and the United Kingdom) and with the participation of ISAS and NASA.

sustainable for a substantial fraction of a Hubble time. These objects are intrinsically important, since, apart from the diffuse intergalactic gas, they comprise the dominant fraction of the baryonic matter in the universe. Perhaps of even more interest for structure formation and extragalactic astronomy is the fact that normal late-type galaxies are the best objects for the investigation of the still poorly understood mechanisms for star formation in galaxian disks, as well as the associated global physical processes and their interrelations.

The deepest statistical investigation of normal galaxies in the local Universe using IRAS was that of Devereux & Hameed (1997) who, after processing the data with the latest techniques, examined the FIR luminosity function at 60 micron for 1215 galaxies within a distance of 40 Mpc, selected from the Nearby Galaxies Catalog of Tully (1989). Even in this catalogue low optical luminosity galaxies and in particular low optical surface brightness galaxies are prone to be under-represented. Furthermore, as discussed by Devereux & Hameed, the sensitivity limit of the IRAS survey meant that only limited information could be derived for the FIR properties of less IR luminous objects and, in particular, of galaxies with almost quiescent star formation activity.

Further obvious biases of IRAS studies in general are the lack of spectral coverage longwards of the $100\ \mu\text{m}$ filter (for which the FWHM system response is approximately 80 - $120\ \mu\text{m}$ - see Fig. II-C-9 of Beichman et al. 1988) and the three times brighter sensitivity limit in this band compared to the IRAS $60\ \mu\text{m}$ band. This could translate into a bias against the detection of FIR emission from quiescent systems, if the $60/100\ \mu\text{m}$ colour ratio is indeed correlated with massive star formation activity as proposed by e.g. Lonsdale & Helou 1987. More fundamentally, the suggestion of Chini et al. (1986) that the spatially integrated spectral energy distribution (SED) of late-type galaxies peaks in the 100 - $200\ \mu\text{m}$ range and cannot be simply extrapolated by fitting the IRAS 60 and $100\ \mu\text{m}$ photometric points with single temperature dust emission components is now confirmed by initial studies with ISO (e.g. Stickel et al. 2000; Popescu et al. 2002).

By virtue of its superior intrinsic sensitivity, and the availability of longer integration times than were possible with IRAS, the ISOPHOT instrument (Lemke et al. 1996) on board ISO (Kessler et al. 1996) could detect discrete sources at least 10 times fainter than IRAS at 60 and $100\ \mu\text{m}$. It furthermore had a wavelength coverage extending to $240\ \mu\text{m}$. The basic observational goal of the project we present here is to use ISO to extend knowledge of the FIR SEDs to lower luminosity limits and to cover the peak in νS_ν for a complete sample of normal late type galaxies, embracing a large range in morphological type and star formation activity.

Ideally, one would seek to achieve this by making a blind survey in the FIR by mapping a substantial fraction of the sky, analogous to IRAS. However, the optimum sensitivity to

luminosity of a detection survey with ISOPHOT was for targets at such a distance that the angular size of the FIR emission region matched the angular resolution of ISO (45 arcsec at 100 micron). For typical dwarf galaxies this corresponds to a distance of about 15 Mpc, so that the low surface number density of such close-by objects would have made a blind survey too costly.

An almost ideal alternative basis for a blind survey in the FIR is offered by the Virgo Cluster Catalogue (VCC), obtained by Binggeli, Sandage & Tammann (1985; hereafter BST85) in their deep blue photographic survey. We therefore selected a sample of late-type galaxies from the VCC catalogue to be observed with ISOPHOT. From an observational point of view the Virgo cluster has the advantage that it is situated at high galactic latitude and is close to the ideal distance for the detection of dwarf galaxies with ISOPHOT. The VCC has a full representation of morphological types of normal gas rich galaxies, including quiescent systems and even, to some extent, low surface brightness objects, ranging from bright ($B_T \sim 10$) giant spirals down to blue compact dwarfs (BCDs) and irregular galaxies at the completeness level of $B_T \sim 18$. Moreover the VCC galaxies are the most carefully classified in terms of optical morphology. Virgo cluster galaxies have been also extensively studied in the UV (Deharveng et al. 1994), optical (e.g. Schröder 1995), H_α , NIR (Boselli et al. 1997a), radio continuum (Gavazzi & Boselli 1999, Niklas, Klein & Wielebinski 1995), HI (Hoffmann et al 1989 & references therein) and CO (e.g. Boselli, Casoli & Lequeux 1995).

From an astrophysical point of view the cluster is ideal in that it is known to be a dynamically young system, with a significant fraction of galaxies freshly falling in from the field (Tully & Shaya 1984, Binggeli, Popescu & Tammann 1993). The fundamental incentive for choosing the VCC as the basis of a statistical sample for ISOPHOT was thus that a luminosity- *and* volume - limited sample of cluster periphery and cluster core galaxies representative of the field and cluster environments, respectively, could be observed down to the least luminous dwarf galaxies reachable with ISOPHOT. This should allow an investigation of the strength and time-dependence of all manifestations of star formation activity and its relation to intrinsic galaxy properties such as Hubble type or sheer overall size. Clusters are natural laboratories for the investigation of the effect on galaxy properties of external conditions such as the pressure and mass density of the diffuse intracluster medium (ICM), the large-scale gravitational potential of the cluster, or the interaction with other galaxies. This is particularly the case for the Virgo cluster for which deep X-ray maps (Böhringer et al 1994) of the ICM, as well as comprehensive measurements of the HI deficiencies (also for dwarf galaxies) are available (Hofmann et al. 1989 and references therein). Another potential manifestation of galaxy-ICM interaction would be the detection of FIR emission in the vicinity of infalling spirals, arising from collisionally heated grains released from the disk through ram-pressure stripping (Dwek, Rephaeli & Mather 1990, Popescu et al. 2000a).

To maximise the statistics attainable in the fixed available observation time of 20.36 hours, the survey was made in just three broad band-passes, centred at 60, 100 and 170 μm , which together encompass the range 40 - 240 μm . In all, a subset of 63 galaxies with $B_T \leq 16.8$ from the VCC were observed. These were selected from specific regions of the sky as described in Sect. 2.

A basic aim of the survey was to derive integrated properties of the sample. This is especially appropriate for cluster samples at a fixed distance to enable the construction of FIR luminosity functions. Furthermore, the angular resolution of ISO (at 100 μm - 4 times superior to that of IRAS) was sufficient to resolve the disks of the giant spirals. This allowed a subsidiary science goal to be realised - namely the provision of statistical information on scale lengths of spiral galaxies in the FIR, their relation to the optical scale lengths, and, to a limited extent, the separation of nuclear and disk emission components. An oversampled scanning technique was used to achieve the combined goals of obtaining integrated fluxes, structural information, and robustness against confusion with background sources or foreground cirrus emission, which limits the survey at the longest wavelength. The use of long scans means that our survey is sensitive to the emission of cold grains in the outer regions of the disks, which are prone to be missed or under-represented in pointed observations of galaxies.

The combination of spatially integrated photometry extending in wavelength to 170 μm will provide the basis for the modelling of the SED of normal galaxies. In this wavelength range grains act as test particles probing the strength and colour of the diffuse UV/optical radiation fields. This constitutes an entirely complementary constraint to direct studies of stellar emission in the UV and optical bands. The SED modelling should yield statistical information on the disk opacities and the relative contributions of young and old stellar populations to the dust heating (see e.g. Xu & Buat 1995; Silva et al. 1998; Devriendt, Guiderdoni & Sadat 1999; Popescu et al. 2000b, Misiriotis et al. 2001). The star formation rate and star formation histories can in principle be derived from such techniques.

Another scientific goal of the survey is to study the statistical correlation of FIR emission of normal disk galaxies with other emissions from the radio to the X-ray spectral regions. In particular, an unexpected result from the IRAS mission was the especially tight correlation between the radio synchrotron and the FIR emission (e.g. Helou, Soifer & Rowan-Robinson 1985, de Jong et al. 1985, Wunderlich, Wielebinski & Klein 1987). The link is qualitatively assumed to be given by the grain heating associated with the appearance of massive stars and the acceleration of relativistic particles in their eventual SN explosions. Basically the correlation can be explained in term of a calorimetric theory (Völk 1989, Lisenfeld, Völk & Xu 1996). One question raised by the IRAS studies is whether the effects of a cluster

environment will indeed shift the FIR/radio - correlation on average to considerably higher radio emission for given FIR intensity as claimed by Gavazzi, Boselli & Kennicutt (1991). Another issue is the extent to which the constraints imposed on galaxian properties by the correlation will apply to less massive and/or more quiescent systems than those typically studied with IRAS.

The sample of VCC galaxies selected for ISOPHOT also formed a substantial part of samples observed with ISO using the ISOCAM MIR camera in pass bands centred at 6.9 and 15 μm (Boselli et al. 1997b, 1998) and the LWS at the 158 μm [CII] fine structure gas cooling line (Leech et al. 1999). In particular, the latter observations provide complementary information about the energetics of the interstellar gas, the sources of [CII] emission within the interstellar medium (Pierini et al. 1999, 2001a), and the role played by different stellar populations in the gas heating (Pierini et al. 2001b).

This paper is organised as follows. In Sect. 2 we describe the selection criteria, optical properties and completeness of the observed sample. Observational details and a description of the data analysis are given in Sections 3 and 4, respectively. The photometric characteristics of the survey, including comparisons with IRAS and COBE photometry, are given in Sect. 5. The extraction of the integrated photometry and the resulting catalogue with associated plots are presented in Sect. 6. Basic properties and detection statistics are derived in Sect. 7 and the main results of the paper are summarised in Sect. 8.

2. The sample

A sample of 62 VCC galaxies selected from the Virgo Cluster Catalogue (BST85) with Hubble type later than S0 was selected according to criteria based on their projected position and magnitude.

The sample galaxies lie in two sky areas called “core” and “periphery”, where the spread in distance within the sample, due to the complex 3D structure of the cluster (Binggeli, Popescu & Tammann 1993 and references therein), is minimised. These areas were chosen in order to optimise the statistical evaluation of the environmental effects of the cluster, if any, on the observed properties of galaxies of the same morphology. It is well-known that galaxies in the cluster core are HI-deficient (Haynes & Giovanelli 1984) while galaxies in the cluster periphery have the same HI content as field galaxies.

The so-called *cluster core subsample* is comprised of 25 certain spiral galaxies brighter than $B_T = 14.5$, with projected positions within 2 degrees of M 87 (Fig. 1), essentially seen towards the extended X-ray halo of M 87 (Böhringer et al. 1994). These galaxies define

an optically complete sample of galaxies later than S0 and earlier than Im. *The cluster periphery subsample* is comprised of 37 spiral, irregular or BCD galaxies with $B_T \leq 16.8$ and with angular separations of greater than 4 degrees from the position of maximum projected galaxy density given by Binggeli et al. (1987) (Fig. 1). Objects with $RA(1950.0) > 12.596^h$ or within 1.5 degree of the position of maximum projected galaxy density of M 49 sub-cluster are excluded. In addition objects seen towards the M and W clouds (as defined in Fig. 1 of Sandage et al (1985) and also reproduced in our Fig. 1) or in the Southern extension ($\delta < 5^\circ$) are also excluded. The limiting magnitude of $B_T = 16.8$ is well within the VCC completeness limit of $B_T \sim 18$. These two subsamples constitute two volume- and magnitude-limited samples of late-type galaxies. The selected galaxies consist of 60 members and 2 possible members (VCC 130 and VCC 890) of the Virgo cluster (Binggeli, Popescu & Tammann).

Due to technical problems with spacecraft operations for some observations, 60 out of the 62 selected VCC galaxies were actually observed with ISOPHOT, giving a statistical completeness of 97%. In particular, all the 25 galaxies of the core subsample and 35 out of the 37 galaxies of the periphery subsample were observed, the two observed subsamples having a statistical completeness of 100% and of 94%, respectively. Hereafter, we refer to the 60 VCC galaxies observed by us with ISOPHOT as the *statistical sample* (marked as circles in Fig. 1).

In addition to this statistical sample, an extended program to observe the remaining 20 cluster member late-type galaxies fainter than $B_T = 14.5$ from the cluster core region was initiated to provide a statistical comparison to faint galaxies (most particularly the Im and BCD galaxies) in the cluster periphery subsample. However, due to scheduling and visibility constraints, only 3 galaxies (VCC 1001, VCC 1121 and VCC 1569) from this extended program were actually observed (marked as crosses in Fig 1).

Table 1 lists the optical and FIR (IRAS) properties of all the 63 VCC galaxies observed by us with ISOPHOT. Our statistical sample includes 7 early-type spiral galaxies with claims of Seyfert/LINER activity or of both (cf. Tab. 1). For VCC 836 (Philips & Malin 1982), VCC 857 (Keel 1983), VCC 1690 and VCC 1727 (Stauffer 1982), these claims were raised before the selection and observation of our statistical sample. On the other hand, VCC 92 (Barth et al. 1998), VCC 1690 and VCC 1727 (Ho, Filippenko & Sargent 1997) have recently been defined as transition spirals, while VCC 857 (Rauscher 1995) and VCC 1043 (Ho, Filippenko & Sargent 1997) seem to be marginal candidates for non-stellar nuclear activity. The phenomenology of Virgo cluster spiral galaxy nuclear regions has not yet been established (e.g. Rauscher 1995), since different types of LINERs (i.e., photoionized by a stellar continuum or by an active galactic nucleus) cannot easily be distinguished from one

another (e.g. Alonso-Herrero, Rieke & Rieke 2000). Given this, we still consider it reasonable to include these 7 VCC spiral galaxies as part of our statistical sample of normal late-type galaxies.

Fig. 2 shows the distribution of the objects of the core and of the periphery subsamples (panels a and b, respectively) in the plane defined by their Hubble type and total apparent blue magnitude B_T . The figure shows that all galaxies in the core subsample and all periphery galaxies brighter than $B_T = 16.5$ were observed (filled symbols). The core and periphery subsamples are thus complete to $B_T = 14.5$ and to $B_T = 16.5$, respectively. It is also evident that the periphery subsample is dominated by spiral galaxies later than Sbc and by irregular or dwarf spiral galaxies, while the core subsample is dominated by spiral galaxies of type Sc and earlier. This behaviour reflects the combination of the morphology–density relation with the morphology–luminosity relation (Sandage, Binggeli & Tammann 1985). In this respect, the two subsamples are complementary, so that our statistical sample represents the overall phenomenology of the *normal* spiral, irregular or dwarf spiral galaxies brighter than $B_T = 16.5$.

3. Observations

All observations were made using ISOPHOT’s “P32” Astronomical Observing Template (Tuffs & Gabriel 2001), which combines the standard spacecraft raster pointing mode (stepping in spacecraft Y and Z coordinates) with scans in Y made with the focal plane chopper. At each spacecraft raster position the focal plane chopper is stepped at intervals of one third of the detector pixel pitch, resulting in sky samplings in Y of ~ 15 and $31''$ for the C100 and C200 detectors, respectively. This is close to the limit for Nyquist sampling of $(17'' \times \lambda)/100 \mu\text{m}$.

The dimension of the spacecraft raster in Y was always made large enough to ensure that the scans spanned the projection of the optical diameters (to the $25.5 \text{ mag arcsec}^{-2}$ B-band isophote) in Y, plus at least one independent resolution element beyond this limit at each scan end. This technique ensured that the survey was sensitive to any infrared emission from a galaxy with as large an extent as the optical extent, while at the same time sampling the target finely enough to probe the basic morphology of the disk emission. These attributes were especially relevant to observations of the bright giant spirals in the sample. A particular aim was to be sensitive to any faint emission from cold dust in the outer disk. Typically, only one spacecraft scan leg was made for the giant spirals. The only exception was the galaxy pair VCC1673/VCC1676, which was mapped in two dimensions, to facilitate the morphological separation of the two systems. The single scan observations

resulted in strip maps of dimension 3 and 2 in the spacecraft Z coordinate for the C100 and C200 detector, respectively, separated by 46 and 92". Although undersampled in Z, the integrated properties of the galaxies could in almost all instances be recovered using the modelling procedures described in Sect. 6. In a few unfavourable cases where the scan direction in spacecraft Y approached being perpendicular to the major axis of the galaxy, some extended emission from the disk was missed.

The oversampling in Y afforded by the P32 mapping technique was also well suited to the fainter targets (generally BCD and irregular galaxies) in the sample, as it mitigated the effects of confusion with the foreground cirrus emission from the Milky Way. To reach the confusion limit integration times were increased for optically faint targets by increasing the dimension of the spacecraft raster in Z, stepping in multiples of the detector pixel pitch so as to ensure that one row of the detector was always scanning through the target. This also improved the precision with which the flat field could be determined. Another problem in the detection of faint sources is the level of residual glitches. Here again, the P32 technique was beneficial to the detection of faint sources as the inherent rapid sampling and redundancy allowed a deeper deglitch, with an efficient rejection of the longer lived responsivity fluctuations which often follow glitch events.

All galaxies were observed in three broad band filters - the C60 and C100 filters on the C100 detector and the C160 filter (which actually has a reference wavelength of 170 μm) on the C200 detector. The C100 filter was chosen in preference to the somewhat more sensitive C90 filter as it provided a more direct comparison with the IRAS 100 μm observations of the brighter galaxies in the sample. This was useful as a check of the calibration (see Sect. 5). The observations of some galaxies were repeated due to operational problems or severe detector instabilities induced by radiation hits. In such cases only the dataset of highest quality was used.

61 of the 63 galaxies were observed in the period May - July 1996. The remaining two galaxies were observed in November 1997. A summary of the basic observational parameters for each target is given in Table 2.

4. Data Reduction

Data was reduced using procedures specifically developed for the analysis of data taken in the "P32" Astronomical Observing Template. These procedures are fully described by Tuffs & Gabriel (2001); here we only outline the major aspects relevant to the present analysis of the Virgo cluster galaxy data. The most important functionality of this new software is

the correction of the transient response behaviour of the Ge:Ga photoconductor detectors of ISOPHOT. As we show below in the context of the present observations, failure to correct for this effect in data taken in the “P32” mode can give rise to serious signal losses and distortions in the derived brightness profiles through the galaxies.

In this paper the data reduction was made outside of the standard PIA (ISOPHOT Interactive Analysis package; Gabriel et al. 1997) program. However, most of the basic operations needed for a photometric calibration of ISOPHOT data - dark current subtraction, correction for integration ramp and signal non-linearity effects, the reset interval correction, and the conversion of engineering units in V/s into astronomical units (MJy sr^{-1}) - utilised subroutines and calibration datasets taken from the standard PIA package. The only exception was the correction for vignetting (see Tuffs & Gabriel 2001). In this work, the calibration is based on the V8.1 release of PIA. There were three principle steps involved in the reduction of “P32” data of the Virgo galaxies: signal conditioning, transient correction and calculation of calibrated transient corrected maps.

4.1. Signal Conditioning

The first step, which is a non-iterative process applied individually to each detector pixel, is **signal conditioning**. This aimed to provide a signal timeline in engineering units free of certain instrumental artifacts, but retaining the complete signature of the transient response of the detector pixel to the illumination history at the full time resolution of the input data. At this stage, the data was corrected for integration ramp non-linearity effects and an orbit dependent dark current was removed. The signal non-linearity correction was not applied prior to the responsivity drift correction.

Information on the actual pointing history of the spacecraft during the observation was extracted and interpolated to the time of each elementary data sample taken during the galaxy observation. This was used to define a rectangular grid of pointing directions on the sky covered by the occurring combinations of chopper and spacecraft pointing positions. Here, the grid spacing was chosen such that the pointing directions were within typically one arcsec of the centre of each grid pixel. As the grid pixels are ~ 15 and 31 arcsec wide in the spacecraft Y coordinate, this removes any need for interpolation or gridding functions when making maps of the sky brightness distribution. We refer to this grid of sky directions as the “P32 natural grid”. An example of the actual pointing directions viewed in detector pixel 1 in an observation with the C100 detector is given in Fig. 3.

The last part of the signal conditioning was the application of P32 specific deglitching

procedures to remove spikes and longer-lived fluctuations in detector responsivity from the data time line. The spike detector was operated individually on the residuals of the data remaining on each chopper plateau after fitting a polynomial to preserve the slower varying transient effects. For bright compact sources observed with the C100 detector, there was evidence for spontaneous glitching when the chopper traversed the direction of peak brightness. Since laboratory investigations on Ge:Ga photoconductors (see Sclar 1984) have shown that this glitching should be preserved as signal, a brightness-dependent threshold for the spike detector was employed to prevent serious signal loss through this effect. Lastly, longer-lived “tails” in the responsivity of detector pixels, often seen following a spike, were identified and flagged by analysing the temporal development of the average level of each chopper plateau viewing a particular sky direction on a given spacecraft pointing. This procedure, which utilises the redundancy afforded by the P32 technique, is the most crucial step determining the instrumental sensitivity, which in the case of the observations of the Virgo galaxies is limited by the degree to which the stochastic undulations in detector responsivity can be removed. In general, removal of these artifacts was virtually complete for the C200 detector, but could only partially be achieved for the C100 detector.

4.2. Transient Correction

Following signal conditioning, the second major step in the data reduction is **transient correction**. This is an iterative process to determine the most likely sky brightness distribution giving rise to the observed signal timeline. It is a non-linear optimisation problem with the values of sky brightness distribution at each point of the P32 natural grid as variables. Iterations are performed involving successive comparisons between the input data time line and a timeline predicted from the convolution of a non-linear detector model with a trial illumination history derived from a trial sky brightness distribution.

The basis for the solution is the empirical model for the transient behaviour of the ISOPHOT C100 and C200 photoconductor detectors described in Tuffs & Gabriel. This involves the superposition of two exponentials, each with illumination dependent time constants. The model also incorporates illumination-dependent jump factors and responsivity coefficients. Each detector pixel has its own constants. As discussed by Tuffs & Gabriel, this model adequately represents the detector response on timescales greater than a few seconds, but only approximately describes the so-called “hook response”. This leads to an over-correction in the photometry (downwards or upwards respectively for decreasing or increasing illumination steps) when the chopper dwell time is shorter than a few seconds. This was the case for the P32 observations of Virgo galaxies which in almost all cases had

chopper dwell times of 0.6 s. Because of the illumination dependence of the detector time constants and jump factors, the effect is more pronounced for decreasing than for increasing illumination steps. For bright sources with a high contrast to the background this induces an asymmetry and a narrowing of the derived brightness profile through a point source compared to the nominal point spread function. Where this was a blatant effect in the drift corrected data timeline, data was censored out manually.

Fig. 4 shows an example of a brightness profile through the faint standard star HR1654 at $100\ \mu\text{m}$, for data processing with and without the responsivity correction. The star has a flux density of 0.52 Jy which would correspond to a medium brightness Virgo galaxy in the sample. Some 95 percent of the flux density has been recovered by the transient correction procedure. Without the correction some 30 percent of the integrated emission is missing and 50 percent of the peak response. The local minimum near 60 arcsec in the Y offset is a typical hook response artifact where the algorithm has overshot the true solution after passing through the source. The actual corrections in integrated flux densities for Virgo galaxies depend on the source brightness, the source/background ratio, and the dwell time on each pointing direction, so there is no fixed correction factor for the photometry. As a rule of thumb, though, brighter more compact galaxies have larger corrections than extended faint sources.

The final part of the transient correction procedure is a reassignment of the uncertainties in the photometry. This is done by examining the scatter in the solutions obtained for each chopper plateau, and is a measure of the irreproducibility of the solution caused by imperfections in the detector model and/or glitch-induced stochastic undulations in the detector responsivity (which, like the white detector noise, are amplified by the transient correction procedure). This procedure yields a more representative measure of the true random uncertainty in the maps than uncertainties derived from the original fits to the integration ramps.

4.3. Calculation of calibrated transient corrected maps

This last stage in the processing starts with the conversion of the transient corrected data from V/s to MJy/sr. For the Virgo cluster galaxies the conversion factors were found individually for each galaxy using the average of the responses for each detector pixel to the fine calibration source exposures made before and after each raster in each filter. Thereafter a time dependent flat field was performed, by examining the time dependence of the detector response to the background directions viewed at the most negative and most positive offsets in Y from the map centre. A flat sky background emission was assumed. For maps with a

single spacecraft raster leg, only a linear time dependence could be fitted. The deeper maps with three scan legs could be fitted with a cubic polynomial.

Maps were made from the transient corrected, calibrated and flat fielded data through a weighted coaddition of the primitive data samples at the full time resolution at each point of the P32 natural grid. Data taken on slews was not used. No gridding function was employed, so that the full angular resolution inherent to the data was preserved. This also means that the measurements at different positions on the map grid are from entirely independent data sets. In cases where there was full detector pixel redundancy in the C100 array (for faint galaxies with at least three scan legs), the coaddition of the data was done first for individual pixels, producing a map cube of 9 maps. Over the region of the P32 natural grid where all 9 maps had data, data from the extreme two detector pixels in the map cube was not used when combining data from all pixels. This acted as a further filter for the glitch-induced undulations in the signal which is the major instrumental source of error. However, this artifact could only be partially removed in this fashion. Many of the final maps appear to exhibit spatially correlated noise at a level greater than predicted by a simple error propagation analysis, which we attribute to residual glitch tails in the data enduring over a series of chopper positions.

The final step is the subtraction of the background. This was done by subtracting a tilted plane obtained from a fit to the extremities of the map (external to the extent of the optical galaxy). In principle, this should provide a better statistical measure of the source brightness near the map centre than subtracting individual baselines from each map row.

5. Evaluation of calibration

The data reduction procedures outlined in Sect. 4 produced maps of Virgo cluster galaxies in surface brightness units calibrated on the ISO flux scale. When comparing ISO data with that from other observatories account should be taken of possible systematic variations in the absolute calibration scale. This section compares the ISO photometry for the Virgo survey with that from COBE-DIRBE and IRAS. This is done firstly by statistically comparing the surface brightnesses of the backgrounds measured by ISOPHOT-C with predictions for these backgrounds derived from the COBE-DIRBE archives. This provides information about the calibration of surface brightness in each of the ISOPHOT C60, C100 and C160 bands. Secondly, a statistical comparison of integrated flux densities of the target galaxies in the C60 and C100 bands with IRAS measurements in the IRAS 60 and 100 μm bands is made. This provides information about the calibration of discrete sources. On the basis of the analysis presented below we decided to calibrate the ISO data on the COBE-DIRBE flux

scale. We give the procedure for the conversion of the ISO brightnesses to the COBE-DIRBE flux scale, as well as conversion factors from COBE-DIRBE to the ISO and IRAS flux scales appropriate for the observations of Virgo cluster galaxies in the P32 mode.

5.1. Comparison of ISO and COBE-DIRBE Background Measurements

Background brightnesses were derived for the 63 VCC galaxies observed by ISOPHOT in each of the COBE-DIRBE bands. The procedure adopted was to average pixels on the DIRBE weekly maps in a circle of radius 1.5 degrees centred on each galaxy, after interpolation to the epoch of each ISOPHOT measurement. The average of these brightnesses was then used to construct a colour-corrected SED of the typical background emission encountered in the cluster in the 25, 60, 100, 140 and 240 μm DIRBE bands (Fig. 5).

Next, the ISOPHOT measurements of the background towards each galaxy were extracted as weighted averages of the P32 maps outside the region enclosed by the 25.5 mag. blue isophote, and colour corrected according to the fitted SED of Fig. 5. The colour corrected ISO backgrounds are plotted versus the colour corrected DIRBE measurements towards each galaxy for each ISOPHOT filter in Fig. 6. Though a good correlation is seen between ISO and COBE-DIRBE at 60 μm , there is a scatter in the ratios, the dispersion becoming more pronounced with increasing wavelength. This might be due either to variations in detector responsivity between different ISOPHOT observations or due to the effect of structured Cirrus emission. We believe that the latter is the most likely explanation, as responsivity variations would be expected to affect both the C60 and C100 measurements in equal measure. Furthermore, particularly in the C160 band, measurements with the highest ISOPHOT/DIRBE ratios are those with the largest dispersion in the background signal between different detector pixels, which one would expect when viewing regions of brighter than average structured Cirrus. Thus, the length of the 1σ bars in the C160 ISO versus DIRBE comparison in Fig. 6c may give an indication of the level of Cirrus confusion in the C160 band.

The systematic differences in the response of ISOPHOT and COBE-DIRBE to the backgrounds are summarised in Table 3. The third column of the table gives brightness values for the fit (Fig. 5) to the mean background, interpolated to the reference wavelengths of the ISOPHOT C60, C100 and C160 filters. The fourth column gives the mean of the ratios of the colour corrected responses of the two instruments to the backgrounds.

Prior to further analysis all ISO data was multiplied by factors of 1.016, 1.185 and 0.885 in the C60, C100 and C160 bands, respectively, in order to bring the ISO measurements

onto the COBE flux scale. This was done primarily because of the remaining intrinsic uncertainties in the absolute ISO calibration. In particular uncertainties in the ramp non-linearity correction for short reset intervals make this approach almost unavoidable. The adoption of the COBE flux scale also provides a basis for cross-calibrating the C100 and C160 detectors, since the spectral coverage of the DIRBE instrument encompasses that of ISOPHOT. The adoption of the COBE-DIRBE flux scale raises appreciably the 100/170 colour temperature of the galaxies in the survey compared with the pure ISO calibration.

This procedure based on the respective responses of ISO and COBE-DIRBE to a smooth background does not necessarily imply a correct adoption of the COBE-DIRBE flux scale for discrete sources. In common with the flux scales of IRAS and COBE-DIRBE, the ISO flux scale is fundamentally based on staring observations of point-like sources (stars, asteroids and planets in the case of ISOPHOT-C), which are subsequently converted into a calibration of surface brightness using measured values for the beam solid angles. To check the validity of the conversion of the ISO flux scale to the COBE-DIRBE flux scale, as described above, a comparison was made between the response of ISO and IRAS to bright Virgo cluster galaxies in their respective 60 and 100 μ m band-passes.

5.2. Comparison of ISO and IRAS photometry of bright galaxies

33 of the 63 galaxies in the ISO sample were detected by IRAS. Although most of these sources were resolved by ISO, they are sufficiently compact (typical IR extent of order of the FWHM of the ISO point spread function) to provide an objective check of the response of the C100 detector to discrete sources. Spatially integrated fluxes were extracted from the ISO maps using the fitting procedure described in Sect. 6 and plotted against the IRAS values at 60 and 100 μ m from Table 1 in Fig. 7a,b.

Except for a few bright galaxies, a good linear correlation is seen between the ISO and IRAS fluxes, consistent with values from the ratio of fluxes measured by ISO to those measured by IRAS of ISO/IRAS = 0.95 and 0.82 at 60 and 100 μ m respectively. The bright

Table 3: Comparison of ISO and DIRBE response to the background

Filter	λ_{ref} (μ m)	Brightness (MJy/sr)	ISO/DIRBE
C60	60	14.59	0.984
C100	100	8.54	0.844
C160	170	6.07	1.130

galaxies with ISO/IRAS ratios well below the correlation were extended objects not well covered in the cross-scan direction. In these cases we attribute the shortfall in integrated flux measured by ISO to the presence of extended emission outside the perimeter of the ISO maps, which could not be fully recovered in the integration of the Gaussian model fits (Sect. 6).

The mean ratio ISO/IRAS for the galaxies in our sample corresponds to the response of ISO to discrete sources relative to that of IRAS, where the ISO measurements have been scaled onto the COBE-DIRBE flux scale. These ratios for discrete sources can be compared to the ratios COBE-DIRBE/IRAS for the background, derived using table IV.D.1 of Wheelock et al. (1994). These background ratios are COBE-DIRBE/IRAS = 0.87 ± 0.05 and 0.72 ± 0.07 in the 60 and 100 μm bands, respectively. Thus, the ratios for the background COBE-DIRBE/IRAS are the same (within the statistical uncertainties) as the ratios ISO/IRAS for discrete sources (0.95 and 0.82, after scaling the ISO measurements onto the COBE-DIRBE flux scale). This validates the basic assumption used to convert the ISO measurements to the COBE-DIRBE flux scale, namely that the scaling factors COBE-DIRBE/ISO derived from background measurements are also valid for discrete sources.

Finally, we note that Odenwald, Newmark & Smoot (1998) found the colour corrected ratio COBE-DIRBE/IRAS for bright galaxies measured by COBE-DIRBE to be 0.94 ± 0.12 and 1.13 ± 0.16 in the 60 and 100 μm bands, respectively. A good agreement with the ISO/IRAS ratios for Virgo galaxies presented here is found in the 60 μm band, but there is a marginal discrepancy in the 100 μm band, where the Odenwald et al. results would suggest that the COBE-DIRBE/IRAS response is significantly greater for discrete sources than for the smooth background. We have no explanation for this discrepancy. However, we do not make explicit use of the COBE/DIRBE response to discrete sources in converting the ISO data to the COBE-DIRBE flux scale.

6. Extraction of photometry

There are two methods to extract the photometry from the data, namely by integrating the raw background-subtracted maps or by fitting a model to the data and then integrating the model to infinity. We applied both methods to our data and show that for this kind of observation the integration of the model to infinity is a more accurate method.

6.1. The integration of the raw maps

The raw integration of the background-subtracted maps has some major disadvantages which make this method less desirable for such analysis. First of all the raw integration of the map will be affected by noise, especially for low surface brightness objects. Secondly this method will not take into consideration any emission that was not included in the scan. This would affect mainly large objects and especially galaxies with large disks scanned along the minor axis, where the map covered only the central part of the galaxy. The FIR emission beyond the scan is usually recovered when fitting a model to the data, except for some extreme cases where the undersampling will also affect the reliability of finding the right parameters for the fit. We nevertheless give flux densities obtained from integration of the raw maps as a first approximation measurement (Table 7).

6.2. The integration of the model fit

The model fit to the data is in principle a more accurate method for extracting the photometry, providing the model is a good description of the true brightness distribution. This method also solves the problems related to the integration of the raw maps. In all cases we fitted 2-dimensional models to the maps, and all models were Gaussians. However it was necessary to fit different combinations of models, according to the different morphologies encountered in the sample, such as single Gaussian fit, two Gaussian fit, multi-component fit, and also a beam fit for point-like sources. Based on the statistics given by the error analysis, we decided on a case by case basis which model better fits the data. We adopted the fitting routines from MINUIT (CERN Program Library) which is a tool to find the minimum value of a multi-parameter function and analyze the shape of the function around the minimum. This tool is especially suited to handle difficult problems, like those which can be encountered in our 2-dimensional maps. It gives very robust results in computing the best-fit parameter values and uncertainties for non-linear problems, taking into account correlations between parameters. This is important in order to have a reliable estimate of the errors in the fitting parameters, to put upper limits on the non-detection, and to detect the presence of a disk or nuclear component in the fit. The flux densities derived from integrating the model fit to infinity are listed in Table 7.

6.2.1. Beam fit

The first step in deriving the photometry is to find a good model for the beam and to evaluate any departure between the model and the true beam. In an ideal case one would have an analytical description of the true beam shape and the integration under a fit to the observations of a true point source would give exactly the same flux density as of the real observation. Unfortunately there is no analytical description of the true shape of the beam. Therefore we describe the beam on the drift-corrected maps as a 2-dimensional circular Gaussian. Because the Gaussian model differs in shape from the true beam profile, the integration to infinity of the best fit to maps is in general systematically different from the true flux densities. To account for this difference it is necessary to correct the model integrated fluxes by some correction factor, f_{corr} . We refer to this correction as the “beam correction”. To determine the value of f_{corr} we fitted simulated noiseless maps of 1 Jy point sources, sampled in exactly the same way as the ISO Virgo maps, with circular Gaussians. The widths of these gaussian beam fit models were $\sigma = 18.56''$, $\sigma = 19.95''$ and $\sigma = 39.49''$ at 60, 100 and 170 μm , respectively, where the Full Width at Half Maximum is $\text{FWHM} = 2.355 \times \sigma$. In all cases the center of the Gaussian was fixed to the center of the map, such that the only free parameter of the fit was the amplitude of the Gaussian. An example of the model fit to the simulated beams is given in Fig. 8. The flux densities obtained from integrating the model fit to infinity were 0.87, 0.84 and 0.87 Jy at 60, 100 and 170 μm , respectively. The flux densities are always below 1 Jy at all three wavelengths, due to the differences between the assumed Gaussian model and the simulated beam. Thus a correction factor was assumed for all flux densities derived from model fits on point sources or on sources which include a point-like source component. The correction factors were $f_{\text{corr}} = 1.149$ at 60 and 170 μm and $f_{\text{corr}} = 1.19$ at 100 μm , where the uncorrected flux densities derived from integrating the model fit have to be multiplied with f_{corr} .

When fitting real Virgo maps of point-like sources with 2-dimensional circular Gaussians we obtained an optimum width for the beam fit model of $\sigma = 17.41''$ at both 60 and 100 μm . The differences between these fit parameters and those obtained for simulated beams are due to the distortions induced in the beam profile by the responsivity drift correction procedure (see Sect. 4.2). For a few cases we found the need to model the beam with a Gaussian having even a smaller width, $\sigma = 15.41''$ at 60 and 100 μm . These latter cases are indicated in all tables with the comment “modified beam”. The effect of decreasing the width of the beam is hardly apparent for the relatively fast C200 detector; therefore at 170 μm we adopted the same width as for the simulated beams. Throughout this paper we refer to the 2-dimensional circular Gaussian model with $\sigma = 17.41''$ at 60 and 100 μm , and $\sigma = 39.49''$ at 170 μm as the “beam fit”.

The flux densities derived from integrating the beam fit model to infinity were then multiplied with the beam correction factors derived from the simulated beams. Presumably these correction factors will give only lower limits for the integrated fluxes, due to the change in the width of the derived profiles at 60 and 100 μm . However we expect the difference between the correction factors derived from simulated beams and the true correction factors which would need to be applied on real observations to be smaller than other uncertainties in the photometry, and we make no attempt to correct for this effect.

The beam fit was utilised for a few galaxies which appeared as point sources, and was also utilised as a way of deriving upper limits for all our non-detections. All such cases are commented as either “beam fit” or “beam fit; non-detection” in the listing of fit parameters in Table 4. For all the other cases the data were fitted by a model which was convolved with the beam fit model. Model fits to the observed brightness profiles of all the Virgo galaxies from our sample are presented in Fig. 10⁶. The brightness scale has been transformed to the COBE-DIRBE scale as described in Sect. 5.

6.2.2. *One Gaussian fit*

Most of our data were fitted by a 2-dimensional elliptical Gaussian, obtained by convolving a model source brightness distribution for each galaxy with a beam fit model, as described in the previous section. The brightness distribution of the source was itself modeled as a 2-dimensional elliptical Gaussian, constrained to have the position angle of the major axis as given by the B band isophotal photometry from the VCC catalogue. Another constraint was to fix the major to minor axial ratio again from the optical data (the VCC catalogue). These constraints were needed because for most of the observations the map extent was only 2 or 3 pixels in the cross-scan direction, and also because of the undersampling problem, which made impossible a reliable determination of the orientation and width of the Gaussian in the cross-scan direction. Such a constraint would nevertheless affect the photometry in cases where the FIR shape of the galaxies would not follow the optical shape of the galaxy.

The center of the Gaussian was fixed to the actual optical centre of the galaxy. This was sometimes slightly offset from the geometrical center of the map due to pointing offsets of the telescope. In many cases the optical position within the map proved to be a poor representation of the actual center of the galaxy in the FIR maps. Therefore an initial fitting routine was used to find the best position of the Gaussians, and this refined position was

⁶This figure is only available for the journal paper.

finally adopted for the fit. Larger shifts from the optical position were mainly found in the C160 maps, probably due to the undersampling of the maps coupled with variation in the responsivity within one map pixel. It is also not unreasonable to consider that part of the shifts are due to real offsets of the optical from the FIR center of the galaxies. The fitted parameters are the amplitude and the width (σ) of the Gaussian. The parameters of the fit are listed in Table 4.

6.2.3. *Two Gaussian fit*

In several cases there was evidence for a nuclear component plus a disk component, which we fitted using a superposition between a beam fit model and a 2-dimensional elliptical Gaussian convolved with the beam fit model. In this case the PA and axial ratio of the disk component were again fixed from the optical data, and the fitted parameters were the amplitude of the nuclear component (the beam fit model) and the amplitude and width of the elliptical Gaussian representing the disk. Again the parameters of the fit are listed in Table 4.

6.2.4. *Multi-component fit*

In a few cases some morphological features were observed in the maps, and therefore a more sophisticated fit was required. Thus for VCC 66, the maps at 60 and 100 microns revealed the presence of a peripheral HII region complex, which we had to fit with a third Gaussian. The galaxies VCC 1554 and VCC 1727 had also to be fitted with a third Gaussian, this time to account for extended emission. The galaxies with multi-component fits are marked in Table 4 as such, and the actual parameters of the fit are given in Table 5.

A special case is the interacting system VCC 1673/VCC 1676. At 60 and 100 μm the observations were twice as finely sampled in the cross-scan direction, resulting in a higher resolution map of the system. These maps could not be fitted by a model, due to the detailed morphologies, and are better suited to the direct integration of the raw maps. Therefore this interacting pair is not included in Fig. 10, but rather will be the object of a separate paper. At 170 μm the sky was undersampled in the cross-scan direction in the same way as for the rest of the galaxies, and thus a model including Four Gaussians was considered. The parameters of this fit are given separately in Table 6.

6.2.5. The χ^2 statistics

The χ^2 statistics reflects the random errors in the fit, being an indicator of the goodness of the fit. In our case χ^2 is also affected by the undersampling in the cross-scan direction. This effect appears simply because the pixel map is supposed to be uniformly illuminated, while our Gaussian model assumes an illumination variation within the pixel. This will be interpreted as a departure between the data and the fit, resulting in an increased χ^2 . For low flux densities the χ^2 will be dominated by the random errors, and the effect of the undersampling is negligible. But with increasing source brightness χ^2 will start to be dominated by the errors resulting from the undersampling, and thus artificially large numbers of the χ^2 will be obtained. This effect is illustrated in Fig. 9 for the flux densities at 60 micron. As expected, for bright sources there is a good linear correlation between the flux densities derived from integrating the model to infinity and the χ^2 of the fit. For faint sources we expect the χ^2 to be dominated by random errors, and thus a scatter diagram is obtained on the left hand side of the plot. For bright sources the real departure between the Gaussian model and the data is given by the scatter in the linear correlation. Thus, for bright sources, the values of the χ^2 had to be corrected for the undersampling effect. The following correlations were used for the correction:

$$\chi^2 = F_{\text{model}} \times 0.70 - 0.5; \quad \text{at } 60 \mu\text{m} \quad (1)$$

$$\chi^2 = F_{\text{model}} \times 0.40 - 0.2; \quad \text{at } 100 \mu\text{m} \quad (2)$$

$$\chi^2 = F_{\text{model}} \times 0.25 - 0.2; \quad \text{at } 170 \mu\text{m} \quad (3)$$

The values of the χ^2 corrected for the undersampling effect are listed in Table 4 (and in Table 5 and 6 for multi-component fit).

6.2.6. Upper limits

In all cases where we had non-detections we derived upper-limits based on beam fits to the data, on the assumption that the galaxy which escaped detection was a point-like source. The upper limits are thus the flux densities corresponding to the 3σ uncertainties in the amplitude of the beam fit model, where the center of the gaussian model was fixed, as described in the previous section. These cases are marked in Table 4 as “beam fit; non-detection”.

We note that the assumption that the undetected galaxies are point-like sources may

not always be true. For low surface brightness extended galaxies the upper limits obtained with our method could be lower than the actual integrated flux density.

7. Detection statistics and basic FIR properties of the sample

From the observed 63 galaxies (61 galaxies observed at all three FIR wavelengths and 2 galaxies observed only at 100 and 170 μm) we have detected 54 (85.7%) galaxies at least at one wavelength and 40 (63.5%) galaxies at all three wavelengths. 9 (14.3%) galaxies were not detected at two wavelengths, namely at 60 and 100 μm , and 5 (7.9%) galaxies were not detected at one wavelength. The 9 galaxies not detected at any wavelength are mainly early type spirals, of SB0 (VCC 984), SBa (VCC 1047) or Sa (VCC 1158) Hubble type, and Im irregulars (VCC 17, VCC 169, VCC 666, VCC 1121). There is also one SBm (VCC 1217) and one Scd: (VCC 1569) which escaped detection. The non-detected early type spirals are bright objects ($12.1 < B_T < 12.8$) in the cluster core while three of the non-detected Im are faint galaxies ($15.2 < B_T < 16.8$) in the cluster periphery.

The statistics of the detections at each wavelength are given in Table 8.

Table 8: Statistics of the detections at individual wavelengths

	60 μm	100 μm	170 μm
detected	41 (67.2%)	43 (68.3%)	54 (85.7%)
observed	61	63	63

The faintest B band galaxy from our sample which was detected at least at one FIR wavelength was VCC 1001. This is an Im galaxy in the cluster core with $B_T = 16.6$ and was detected only at 170 μm . (The galaxy was not observed at 60 μm and was not detected at 100 μm .) The derived flux at 170 μm is 0.23 ± 0.03 Jy. The galaxy has an extremely cold dust emission and we will discuss its properties in a subsequent paper. The faintest B band galaxies from our sample which were detected at least at two FIR wavelengths were VCC 130 and VCC 1750, two BCDs in the cluster periphery with $B_T = 16.5$. Both galaxies were detected only at 100 and 170 μm . VCC 1750 reached 0.04 ± 0.01 and 0.08 ± 0.02 Jy at 100 and 170 μm , respectively.

The faintest detected emission at 60 μm is 0.05 ± 0.01 Jy (detected in VCC 1675, a peculiar galaxy in the cluster periphery, and in VCC 1725, a Sm/BCD galaxy also in the cluster periphery). The faintest detected emission at 100 μm is 0.04 ± 0.01 Jy (detected in VCC 1750, one of the two galaxies which were also assigned as being the faintest B band

galaxies detected at least at two FIR wavelengths). Finally the faintest detected emission at $170\ \mu\text{m}$ is $0.08 \pm 0.02\ \text{Jy}$ (detected in VCC 130 and in VCC 1750, which were also the faintest B band galaxies detected at least at two FIR wavelengths). For comparison the faintest detected IRAS emission on the galaxies from our sample is $0.2\ \text{Jy}$ (VCC 459, VCC 1410, VCC 1757) at $60\ \mu\text{m}$ and $0.4\ \text{Jy}$ (VCC 1757) at $100\ \mu\text{m}$. Thus our survey can go $10 - 20$ times deeper (at $100\ \mu\text{m}$) than the IRAS survey.

The faintest upper limits (defined as 3σ errors) assigned to the galaxies in our sample are $0.03\ \text{Jy}$ at $60\ \mu\text{m}$ (VCC 169, VCC 666, VCC 1581, VCC 1750), $0.02\ \text{Jy}$ at $100\ \mu\text{m}$ (VCC 1001, VCC 1121) and $0.04\ \text{Jy}$ at $170\ \mu\text{m}$ (VCC 666). For comparison the faintest upper limits assigned by IRAS to the galaxies from our sample are 0.2 and $0.5\ \text{Jy}$ at 60 and $100\ \mu\text{m}$, respectively. Thus our survey assigns upper limits which are again ~ 20 times fainter (at $100\ \mu\text{m}$) than those assigned by the IRAS survey. The averaged 3σ upper limits of the galaxies (point sources) from our sample were 43 , 33 and $58\ \text{mJy}$ at 60 , 100 and $170\ \mu\text{m}$, respectively.

Interestingly, the highest detection rates were for the C160 band, even for dwarfs, despite the detection limit in terms of Jy being about twice as bright as the C100 and C60 detection limits. Particularly for BCDs it was not obvious that this was to be expected.

The galaxies with the brightest FIR fluxes are VCC 1673/VCC 1676, which form an interacting system with total integrated flux densities of 11.32 ± 0.19 , 29.34 ± 0.46 and $96.85 \pm 1.56\ \text{Jy}$ at 60 , 100 and $170\ \mu\text{m}$, respectively.

From the observed 63 galaxies, 21 (33.3%) galaxies present evidence for a nuclear and a disk component at least at one wavelength and 4 (6.3%) galaxies present evidence for a multi-component morphology at least at one wavelength.

The flux density distributions at 60 , 100 and $170\ \mu\text{m}$ are given in Fig. 11 . There is an obvious shift of the right hand side of the histogram towards larger fluxes with increasing wavelength. The distribution at $170\ \mu\text{m}$ is slightly broader than the distribution at 60 , and $100\ \mu\text{m}$ due to the larger completeness of the sample at longer wavelengths. Some faint galaxies detected at $170\ \mu\text{m}$ failed detection at $60\ \mu\text{m}$, producing the cut in the faintest side in the histogram at $60\ \mu\text{m}$.

8. Summary

63 spiral, irregular and dwarf galaxies in the Virgo cluster have been observed down to the limiting sensitivity of the ISOPHOT instrument on board ISO in band-passes centred on

60, 100 and 170 micron. Rapid oversampled scans covering the entire optical extent of each target down to the $25.5 \text{ mag arcsec}^{-2}$ B-band isophote and adjacent background directions were made using ISOPHOT's focal plane chopper in conjunction with a spacecraft raster. For the first time, data taken in this mode could be corrected for the complex non-linear response to the illumination history in each observation. This allowed robust integrated photometry and structural information to be extracted down to the confusion limit in the 170 micron band and to the sensitivity limits imposed by low-level glitching in the 60 and 100 micron bands.

The photometry in the 60 and $100 \mu\text{m}$ bands was found to be well correlated with the corresponding IRAS measurements for the 33 of the 63 galaxies detected by IRAS, with relative gains $\text{ISO/IRAS} = 0.95$ and 0.82 at 60 and $100 \mu\text{m}$ respectively.

The faintest detected emissions from our galaxy sample were 50, 40 and 80 mJy at 60, 100 and $170 \mu\text{m}$, respectively. The faintest 3σ upper limits for integrated flux densities were 30, 20 and 40 mJy (at 60, 100 and $170 \mu\text{m}$). The averaged 3σ upper limits (of galaxies with pointlike source appearance) were 43, 33 and 58 mJy (at 60, 100 and $170 \mu\text{m}$). 54 galaxies (85.7%) were detected at least at one wavelength, and 40 galaxies (63.5%) were detected at all three wavelengths. The highest detection rate (85.7%) was in the $170 \mu\text{m}$ band.

From the observed 63 galaxies, 21 (33.3%) presented evidence for a nuclear and a disk component at least at one wavelength and 4 (6.3%) galaxies presented evidence for a multi-component morphology at least at one wavelength.

The data presented in this paper were taken in guaranteed observing time made available by the ISOPHOT PI D. Lemke and the ISO Project Scientist M.F. Kessler. We thank U. Klein, J. Lequeux and B. Binggeli for advice and discussions concerning the selection of galaxies observed, D. Skaley for assistance in entering the observing parameters into the uplink database, S. Niklas for support in the initial stages of the data evaluation, P. Abraham and the ISOPHOT data centre for advice and assistance in the photometric comparison between ISO and COBE/DIRBE, and the staff of the ISO data centre at Villafranca for advice on calibration and data analysis issues. RJT thanks B. Madore for hospitality at the Observatories of the Carnegie Institution of Washington during the preparation of this paper. This project was supported by grant 50 QI 9201 of the DLR.

This research has made use of the NASA/IPAC Extragalactic Database (NED) which is operated by the Jet Propulsion Laboratory, California Institute of Technology, under contract with the National Aeronautics and Space Administration.

REFERENCES

- Alonso-Herrero, A., Rieke, M. J., Rieke, G. H. 2000, ApJ, 530, 688
- Barth, A. J., Ho, L. C., Filippenko, A. V., Sargent, W. L. W., 1998, ApJ, 496, 133
- Beichman, C. A., Neugebauer, G., Habing, H. J., Clegg, P. E., & Chester, T. J. (Eds.), 1988
IRAS Catalogs and Atlases: Explanatory Supplement (NASA RP-1190)
- Binggeli, B., Sandage, A. & Tammann, G. A. 1985, (BST85) AJ, 90, 1681
- Binggeli, B., Tammann, G. A., Sandage, A. 1987, AJ 94, 251
- Binggeli, B., Popescu, C. C., Tammann, G. A. 1993, A&AS, 98, 275
- Böhringer, H., Briel, U. G., Schwarz, R. A., Voges, W., Hartner, G., & Trümper, J. 1994,
Nature, 368, 828
- Boselli, A., Casoli, F. & Lequeux, J. 1995, A&AS, 110, 521
- Boselli, A., Lequeux, J., Contursi, A., Gavazzi, G., Boulade, O., Boulanger, F., Cesarsky,
D., Dupraz, C., Madden, S., Sauvage, M., Viallefond, F., & Vigroux, L. 1997b, A&A,
324, L13.
- Boselli, A., Tuffs, R. J., Gavazzi, G., Hippelein, H., & Pierini, D. 1997a, A&AS, 121, 507.
- Boselli, A., Lequeux, J., Sauvage, M., Boulade, O., Boulanger, F., Cesarsky, D., Dupraz, C.,
Madden, S., Viallefond, F., & Vigroux, L. 1998, A&A, 335, 53
- Chini, R., Kreysa, E., Krügel, E., Mezger, P. G. 1986, A&A, 166, L8
- de Jong, T., Klein, U., Wielebinski, R., & Wunderlich, E. 1985, A&A, 147, L6
- Deharveng, J. -M., Sasseen, T. P., Buat, V., Bowyer, S., Lampton, M., Wu, X. 1994, A&A,
289, 715
- Delgado, G., Rosa, M., Pérez, E., Tadhunter, C., Vilchez, J. M., & Rodríguez-Espinosa J.
M. 1997, ApJS, 108, 155
- Devriendt, J. E. G., Guiderdoni, B., & Sadat, R. 1999, A&A, 350, 381
- Devereux, N. A. & Hameed, S. 1997, AJ, 113, 599
- Dwek, E., Rephaeli, Y., Mather, J. C. 1990, ApJ, 350, 104

- Gabriel, C., Acosta-Pulido, J., Heinrichsen, I., Morris, H., Skaley, D. & Tai, W -M, 1997; in
proc. "Data Analysis in Astronomy", Eds. V. Di Gesu, M. J. B., Duff, A., Heck, M.
C., Maccarone, L., Scarsi & H. U., Zimmerman. World Scientific Press, 1997, p. 409
- Falcke, H., Wilson, A. S., Simpson, C. 1998, ApJ, 502, 199
- Gavazzi, G. & Boselli, A. 1999, A&A, 343, 86
- Gavazzi, G., Boselli, A., & Kennicutt, R. 1991, AJ, 101, 1207
- Haynes, M. P., Giovanelli, R. 1984, AJ, 89, 758
- Helou, G., Khan, I. R., Malek, L., & Boehmer, L. 1988, ApJS, 68, 151
- Helou, G., Soifer, B. T., & Rowan-Robinson, M. 1985, ApJ, 298, L7
- Ho, L. C., Filippenko, A. V., Sargent, W. L. W. 1997, ApJS, 112, 315
- Hoffmann, G. L., Williams, H. L., Salpeter, E. E., Sandage, A., & Binggeli, B. 1989, ApJS,
71, 701
- Keel, W.,C. 1983, ApJS, 52, 229
- Kessler, M. F., Steinz, J. A., Anderegg, M. E., Clavel, J., Drechsel, G., Estaria, P., Fälker,
J., Riedinger, J. R., Robson, A., Taylor, B. G., Ximenéz de Ferrán, S. 1996, A&A,
315, 27
- Klatt, U. 1993, Diploma thesis, University of Heidelberg
- Leech, K. J., Rowan-Robinson, M., Lawrence, A., Hughes, J. D. 1994, MNRAS 267, 253
- Leech, K. J., Völk, H. J., Heinrichsen, I., Hippelein, H., Metcalfe, L., Pierini, D., Popescu,
C. C., Tuffs, R. J., & Xu, C. 1999, MNRAS, 310, 317
- Lemke, D., Klaas, U., Abolins, J., Ábráham, P., Acosta-Pulido, J., Bogun, S., Castañeda,
H., Cornwall, L., Drury, L., Gabriel, C., Garzón, F., Gemünd, H. P., Grözing, U.,
Grün, E., Haas, M., Hajduk, C., Hall, G., Heinrichsen, I., Herbstmeier, U., Hirth, G.,
Joseph, R., Kinkel, U., Kirches, S., Kömpe, C., Krätschmer, W., Kreysa, E., Krüger,
H., Kunkel, M., Laureijs, R., Lützow-Wentzky, P., Mattila, K., Müller, T., Pacher,
T., Pelz, G., Popow, E., Rasmussen, I., Rodríguez Espinosa, J., Richards, P., Russell,
S., Schnopper, H., Schubert, J., Schulz, B., Telesco, C., Tilgner, C., Tuffs, R. J., Völk,
H. J., Walker, H., Wells, M., Wolf, J. 1996, A&A, 315, L64
- Lisenfeld, U., Völk, H. J., & Xu, C. 1996, A&A, 306, 677

- Lonsdale, C. J. & Helou, G. 1987, *ApJ*, 314, 513
- Misiriotis, A., Popescu, C. C., Tuffs, R. J., Kylafis, N.D. 2001, *A&A* 372, 775
- Moshir, M., Kopan, G., Conrow, T., et al. 1990, “IRAS Faint Source Catalogue”, version 2.0
- Niklas, S., Klein, U. & Wielebinski, R. 1995, *A&A*, 293, 56
- Nilson P. 1973, “Uppsala General Catalogue of Galaxies”, *Nova Acta Regiae Soc. Sci. Upsaliensis*, Ser. V:A, 1 (UGC)
- Odenwald, S., Newmark, J. & Smoot, G. 1998, *ApJ*, 500, 554
- Phillips, M. M., Malin, D. F. 1982, *MNRAS*, 199, 905
- Phillips, M. M., Charles, P. A., Baldwin, J. A. 1983, *ApJ*, 266, 485
- Pierini, D., Leech, K. J., Tuffs, R. J., & Völk, H. J. 1999, *MNRAS*, 303, 29.
- Pierini, D., Lequeux, J., Boselli, A., Leech, K. J., & Völk, H. J. 2001a, *A&A*, 373, 827
- Pierini, D. et al. 2001b, submitted
- Popescu, C. C., Tuffs, R. J., Fischera, J. & Völk, H. J. 2000a, *A&A*, 354, 480
- Popescu, C. C., Misiriotis, A., Kylafis, N. D., Tuffs, R. J. & Fischera, J. 2000b *A&A*, 362, 138
- Popescu, C. C., Tuffs, R. J., Völk, H. J., Pierini, D., Madore, B. F. 2002, *ApJ* in press
- Rauscher, B. J., 1995, *AJ*, 109, 1608
- Sandage, A., Binggeli, B., Tammann, G.,A. 1985, *AJ*, 90, 1759
- Sanders, D. B. & Mirabel, I.,F. 1996, *ARAA*, 34, 749
- Silva, L., Granato, G.,L., Bressan, A., & Danese L. 1998, *ApJ*, 509, 103
- Soifer, B. T., Neugebauer, G., & Houck, J. R. 1987, *ARAA*, 25, 187
- Stauffer, J. R. 1982, *ApJ*, 262, 66
- Stickel, M., Lemke, D., Klaas, U., Beichman, C. A., Rowan-Robinson, M., Efstathiou, A., Bogun, S., Kessler, M. F., & Richter, G. 2000, *A&A*, 359, 865

- Schröder, A. 1995, PhD thesis, University of Basel
- Sciar, N. 1984, in *Prog. Quant. Electr.* 9, 149
- Tammann, G. A. & Sandage, A. 1985, *ApJ*, 294, 81
- Thuan, T. X & Sauvage, M. 1992, *A&AS*, 92, 749
- Tuffs, R. J. & Gabriel, C. 2001, *A&A*, in preparation
- Tully, R. B. & Shaya, E. J. 1984, *ApJ*, 281, 31
- Tully, R. B. 1989, “Nearby Galaxies Catalog”, Cambridge University Press, Cambridge
- Völk, H. J. 1989, *A&A*, 218, 67
- Wheelock, S. L., Gautier, T. N., Chillemi, J., Kester, D., McCallon, H., Oken, C., White, J., Gregorich, D., Boulanger, F. & Good, J. 1994, *IRAS sky survey atlas: Explanatory supplement*
- Wunderlich, E., Wielebinski, R., & Klein, U. 1987, *A&AS*, 69, 487
- Xu, C. & Buat, V. 1995, *A&A*, 293, L65

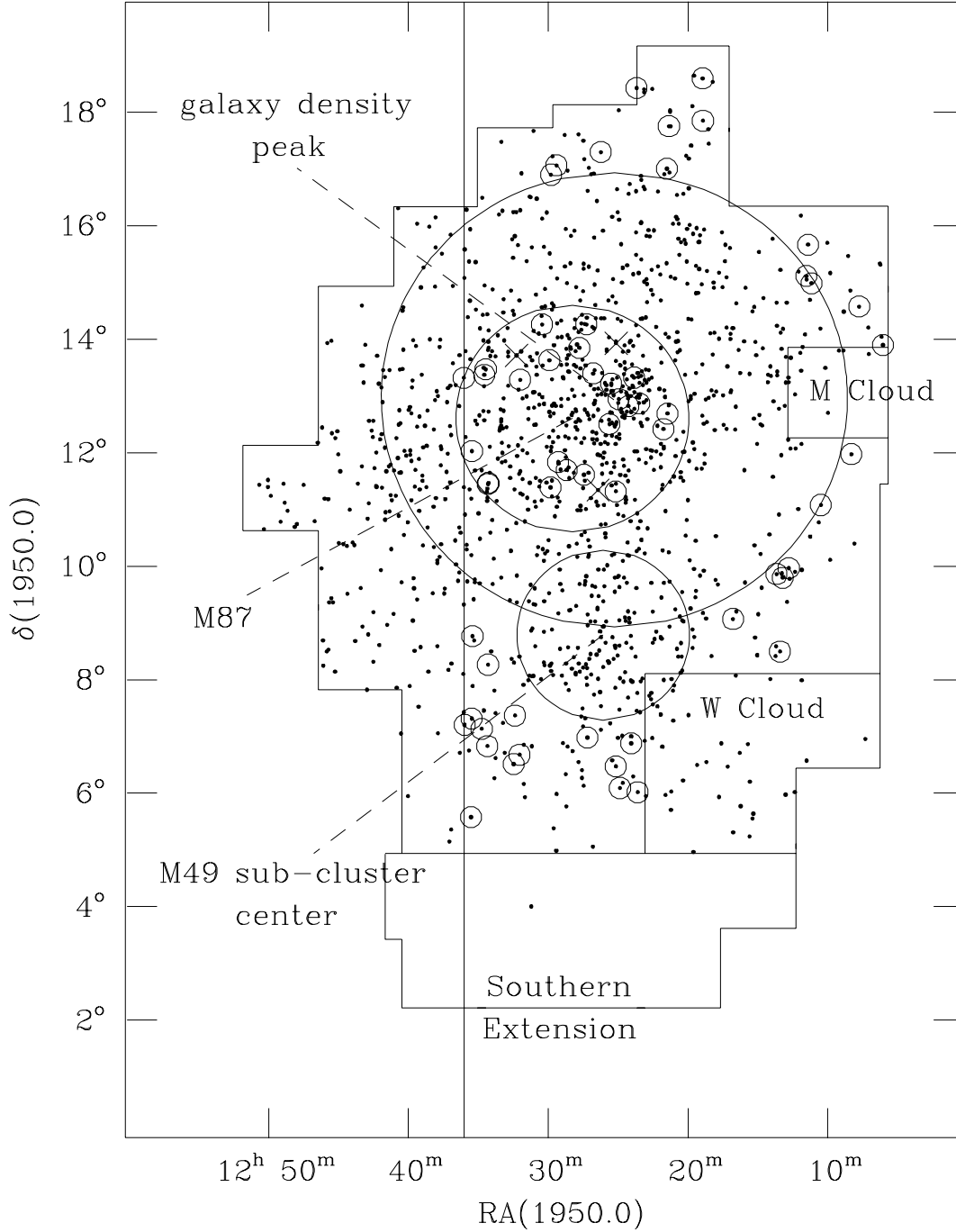


Fig. 1.— Plot of the VCC member galaxies (dots), as defined by BST85 and Binggeli, Popescu & Tammann (1993), with the cluster topology as given by Sandage, Binggeli & Tammann (1985). The 60 VCC galaxies of the statistical sample and the 3 VCC galaxies of the extended sample observed by us are marked with open circles and crosses, respectively. The Figure also show the 4° radius region centered on the maximum projected galaxy density of the cluster (Binggeli, Sandage & Tammann 1987), the 2° radius region centered on M87, the 1.5° radius region centered on the position of the maximum projected density of the M49 sub-cluster and the boundary line at $RA(1950.0) = 12.596^h$ (see text).

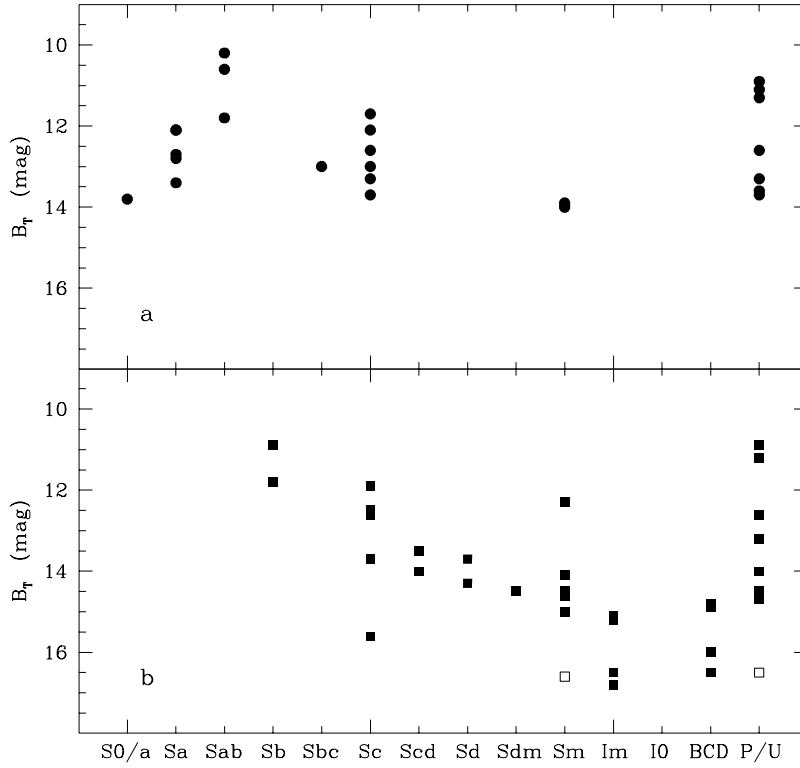


Fig. 2.— The galaxy bivariate distribution in the plane defined by morphological type and total apparent magnitude B_T , as listed in the VCC, for the core subsample (a) and the periphery subsample (b). In each panel, the last morphological bin “P/U” contains either peculiar galaxies or objects of uncertain morphology. Circles and squares denote objects in the core and periphery subsamples, respectively. Empty squares denote galaxies in the cluster periphery subsample not observed by ISOPHOT (see text).

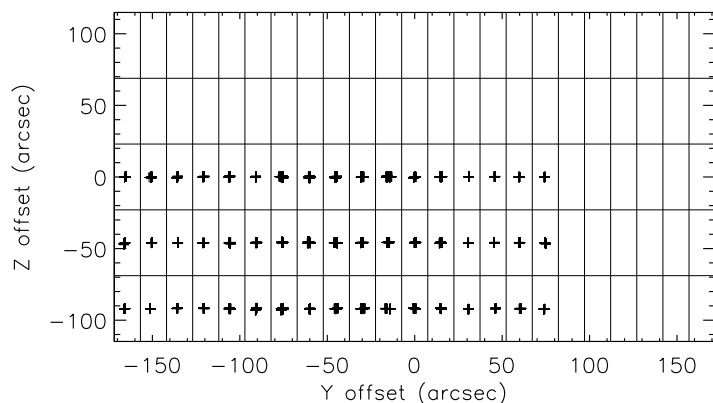


Fig. 3.— Pointing directions observed towards VCC 1 at $60\mu m$ in detector pixel 1. The spacecraft raster dimension was 2×3 in $Y \times Z$. Each pointing direction for 3509 individual data samples for the central pixel of the C100 detector array is plotted as a cross. The rectangular grid is the “P32 natural grid” (see text) for this observation, on which the sky brightness distribution is to be solved. The grid sampling is 14.94×45.95 arcsec. The registration of chopper and spacecraft pointing, and the inherent pointing stability of ISO allow the data samples to be typically within 1 arcsec of the centre of each pixel of the P32 natural grid.

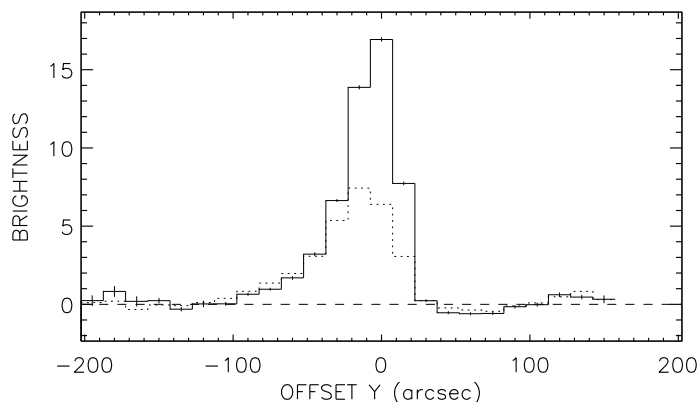


Fig. 4.— Brightness profiles along the Y spacecraft scanning direction (raster and chopper scan from right to left) through the standard star HR1654 at $100\mu m$. The solid line represents data analysed in the same manner as the target Virgo cluster galaxies, while the dotted line represents data with identical processing but without the responsivity drift correction.

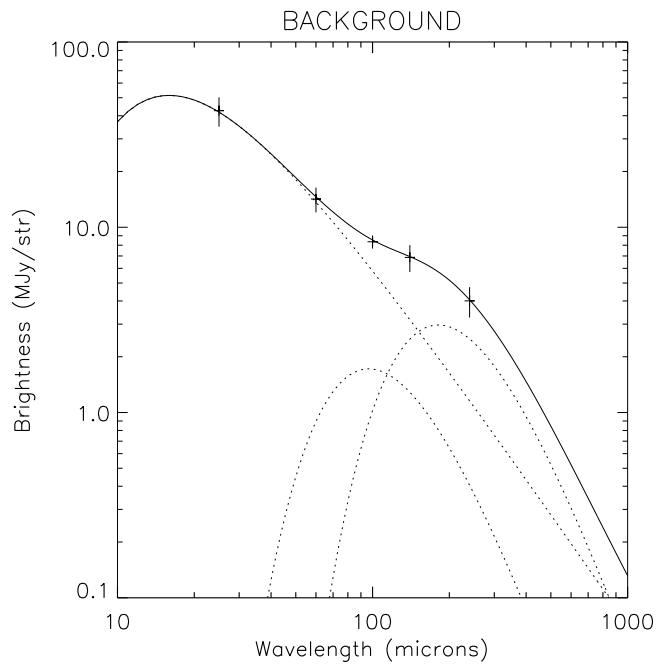
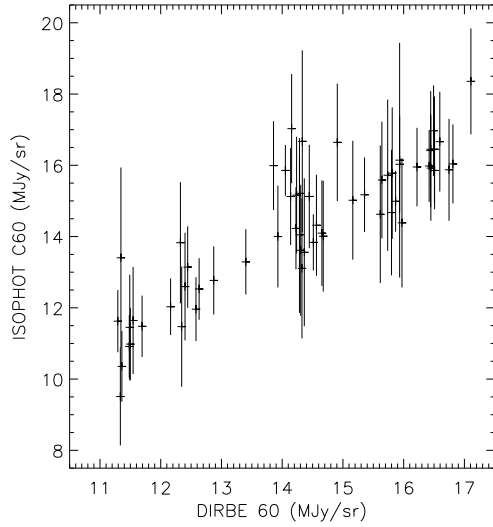
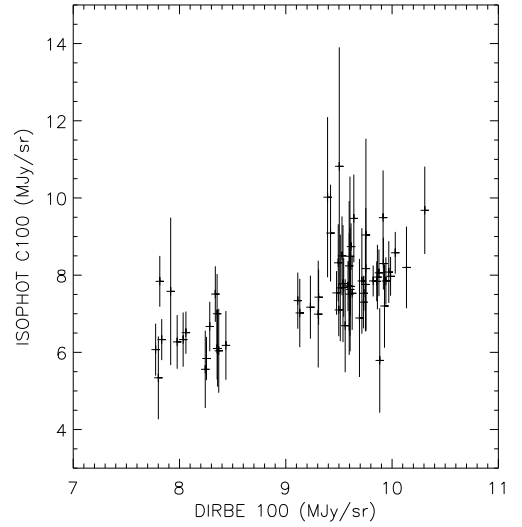


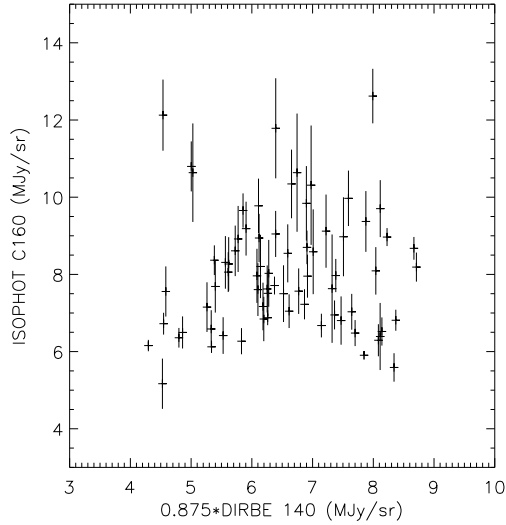
Fig. 5.— The SED of the background emission seen towards the positions of the target galaxies, as measured by COBE-DIRBE. The vertical bars delineate the 1σ spread in DIRBE brightnesses measured at the target galaxies, and the horizontal line denotes the average of these measurements. The solid line represents a fit to the average brightnesses composed of the sum of three spectral components denoted by the three dotted curves: a black body spectrum with $T=320\text{K}$ for the zodiacal component, and modified ($m=2$) black body spectra with $T=30$ and $T=16$ K for the foreground galactic dust emission. The DIRBE data were colour corrected according to the fitted SED.



(a)



(b)



(c)

Fig. 6.— ISO backgrounds in the three ISOPHOT filters versus colour corrected brightnesses derived from DIRBE weekly maps in the 60, 100 and 140 μm bands towards the positions of each target galaxy. The DIRBE measurements were interpolated to the epoch of each ISO observations. Colour corrections were applied according to the fit to the mean DIRBE SED of Fig. 5. For the C160 filter, the DIRBE data was multiplied by 0.875, which is the factor by which the fit to the colour corrected background SED decreases between the DIRBE reference wavelength (140 μm) and the reference wavelength of the C160 filter (170 μm). The vertical bars represent the 1σ dispersion in the response of individual detector pixels on ISOPHOT-C to the background.

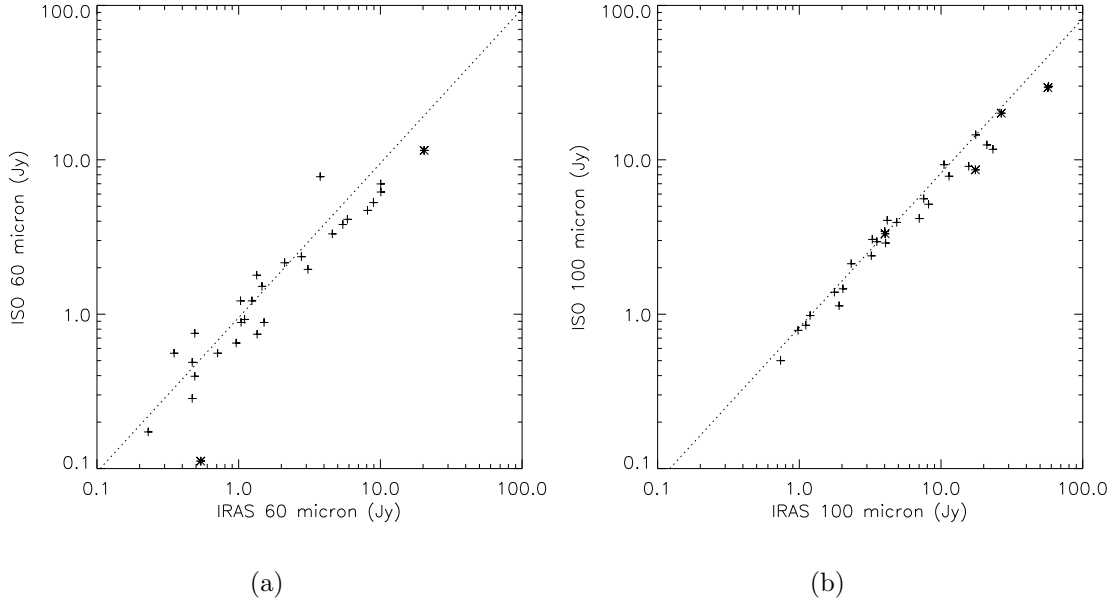


Fig. 7.— a) Integrated and colour corrected flux density of galaxies measured in the ISO C60 filter versus integrated colour corrected flux densities measured by IRAS in its $60\ \mu\text{m}$ band. The colour correction factors were applied assuming the SED of the galaxies could be approximated by the superposition of two modified ($m=2$) Planck curves with temperatures 16 and 30 K with the same relative amplitude as used in Fig. 5 for the fitting of the foreground dust emission from the Milky way seen towards the Virgo cluster. b) the same but for the ISO C100 filter and the IRAS $100\ \mu\text{m}$ band. The ISO data represent the spatial integration of Gaussian components fitted as described in Sect. 6, and scaled to the COBE flux scale as described in Sect. 5. In each panel the dotted line is not a fit to the correlation, but represents the relation a) $\text{ISO}/\text{IRAS}=0.95$; b) $\text{ISO}/\text{IRAS}=0.82$ obtained in Sect. 5.2. The star symbols represent the integrated emission on the maps of a) VCC 1253, and VCC 1673; b) VCC 873, VCC 1379, VCC 1673 and VCC 1690, rather than the integration of the model fits. The galaxies plotted with stars have large χ^2 for the model fit (see Table 4).

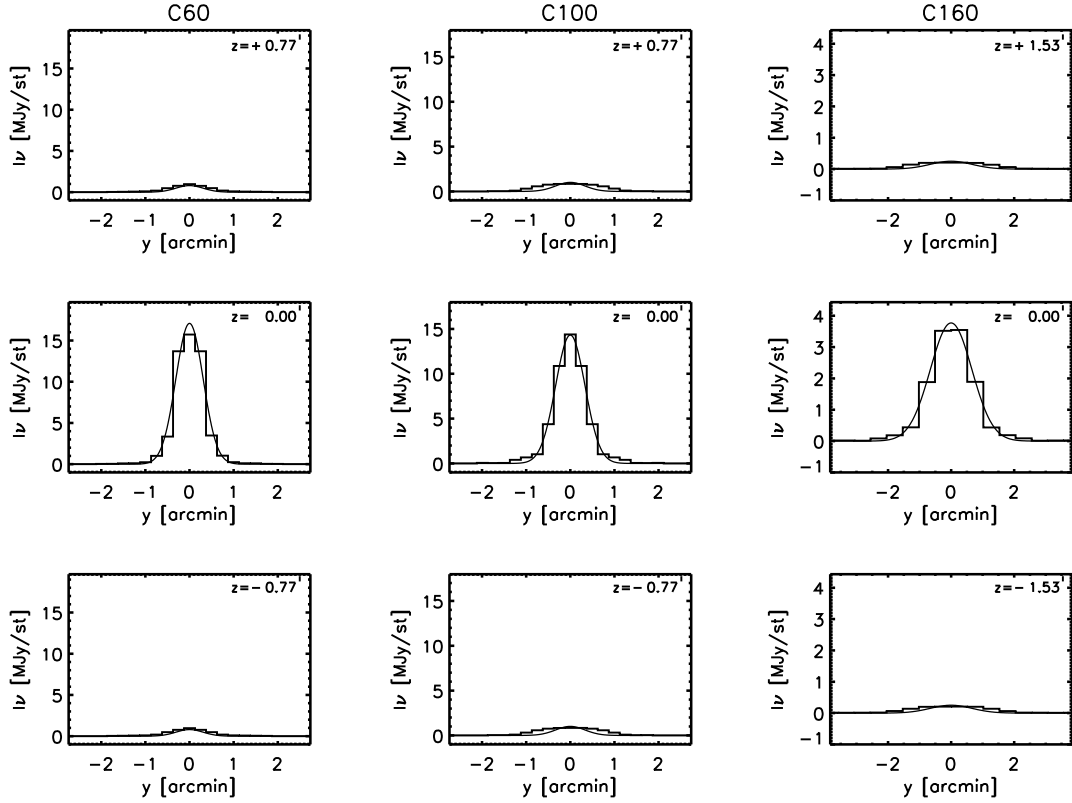


Fig. 8.— Example of a beam fit on simulated noiseless maps of 1 Jy point sources, sampled in the exactly the same way as the ISO Virgo maps. The simulated beams are plotted as histograms while the model fits are plotted as solid lines. The left, middle and right columns give the fits to the 60, 100 and 170 μm maps, respectively. The middle row gives the fits to the central map row (the profile along the scan direction), while the upper and the lower rows give the fits to the neighbouring map rows. The shift in cross-scan direction z between the central and the neighbouring rows is indicated in each panel.

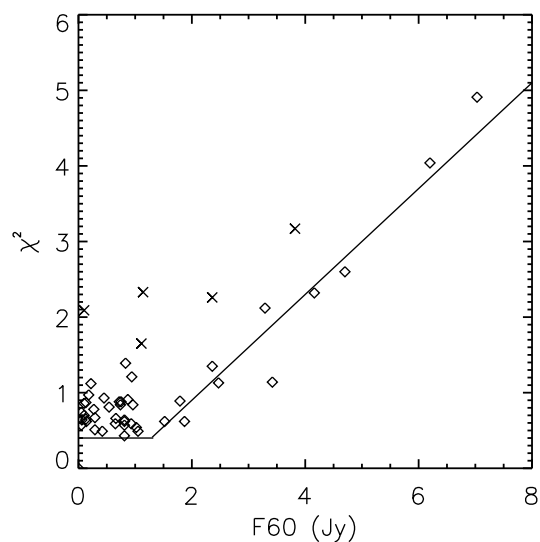
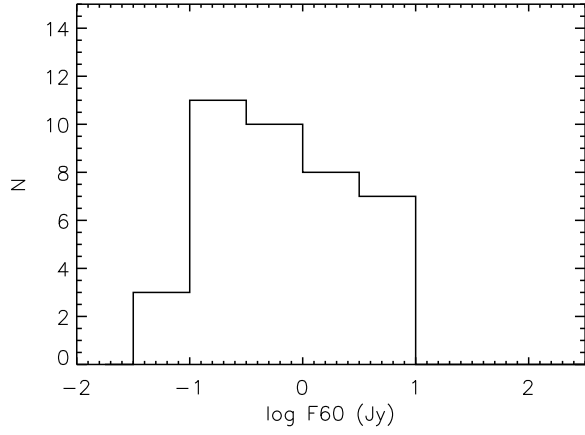
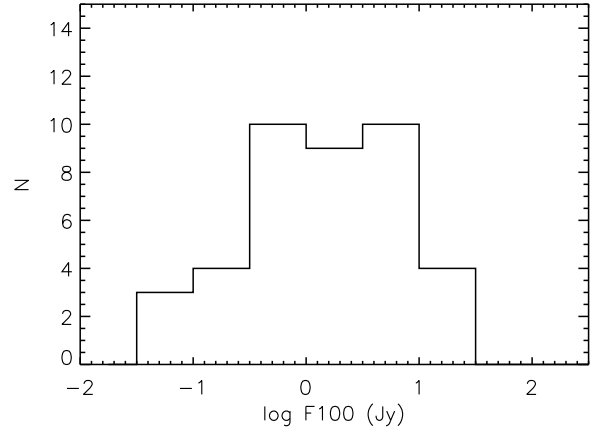


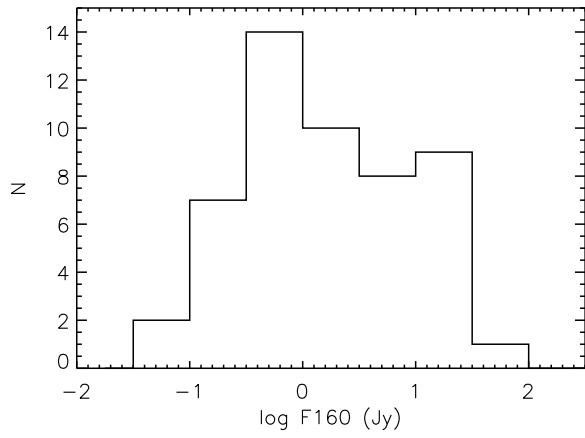
Fig. 9.— The uncorrected χ^2 values derived from fitting the Gaussian models to the maps versus the corresponding flux densities at $60\mu\text{m}$ obtained from integrating the model fit to infinity. The data were plotted as diamonds, except for those galaxies for which the model was an imperfect fit to the data, which were plotted as stars. The solid line rising for $F60 > 1.5\text{ Jy}$ represents the linear correlations between flux and χ^2 , as a result of systematic errors due to the oversampling in cross-scan direction. For faint flux densities χ^2 is dominated by systematic errors, producing a clumpy distribution at the left hand side of the plot, with a lower envelope, which we traced by a solid line to guide the eyes.



(a)



(b)



(c)

Fig. 10.— The flux density distributions at 60, 100 and 170 μm .

Table 1. Galaxy parameters

VCC	Other denomination	C/P ^a	$\alpha(2000.0)$ hh mm ss	$\delta(2000.0)$ ° ' "	D ^b '	R ^c	PA ^d deg	type	B _T mag	F60 ^e Jy	F100 Jy	notes
1		P	12 08 20.3	13 41 03	0.8	4.3	0	BCD?	14.8			
17		P	12 10 01.8	14 22 00	1.4	2.0	0	Im	15.2			
24		P	12 10 35.6	11 45 39	0.8	2.7	0	BCD	14.9			
66	NGC 4178, UGC 7215	P	12 12 46.5	10 52 06	6.6	2.8	30	SBc	11.9	2.8	9.0	HII
81	NGC 4192A, UGC 7223	P	12 13 26.2	14 46 20	1.8	1.2	0	d:Sc	15.6			
87		P	12 13 41.3	15 27 13	1.8	2.0	0	Sm	15.0			
92	M 98, NGC 4192, UGC 7231	P	12 13 48.3	14 54 01	12.0	3.7	155	Sb:	10.9	6.5	21.5	HII, LINER ^{g,h}
130		P	12 15 04.0	9 45 13	0.4	2.5	0	BCD	16.5			
152	NGC 4207, UGC 7268	P	12 15 30.4	9 35 09	2.3	2.2	124	Scd	13.5	2.9	7.4	
159		P	12 15 41.5	8 17 08	0.9	2.0	0	Im	15.1			
169		P	12 15 56.4	9 38 56	1.0	2.0	0	Im	16.5			
318	IC 776, UGC 7352	P	12 19 02.9	8 51 22	2.1	1.7	98	SBcd	14.0			
459		P	12 21 11.2	17 38 18	0.6	2.3	0	BCD	14.9	0.2	0.5	
460	NGC 4293, UGC 7405	P	12 21 12.8	18 22 57	6.3	1.7	72	Sa pec	11.2	4.6	10.4	
655	NGC 4344, UGC 7468	P	12 23 37.5	17 32 27	1.4	1.0	0	S pec/BCD	13.2	0.4	1.9	
664	IC 3258, UGC 7470	C	12 23 44.5	12 28 42	3.2	1.4	0	Sc	13.7	0.5	0.7	
666		P	12 23 46.1	16 47 29	1.3	1.7	0	Im:	16.8			
692	NGC 4351, UGC 7476	C	12 24 01.6	12 12 18	3.6	1.5	80	Sc	13.0	0.6	2.1	
836	NGC 4388, UGC 7520	C	12 25 46.7	12 39 44	6.3	4.1	92	Sab	11.8	10.1	17.4	Sy2 ^{i,j,k}
848		P	12 25 52.5	5 48 33	1.4	1.2	0	Im pec/BCD	14.7			
857	NGC 4394, UGC 7523	P	12 25 55.7	18 12 49	4.5	1.0	0	SBb	11.8	1.0	4.0	LINER ^{g,l}
873	NGC 4402, UGC 7528	C	12 26 07.7	13 06 48	4.9	3.4	90	Sc	12.6	5.4	17.4	
890		P	12 26 21.5	6 40 10	0.1	1.0	0	BCD	16.0			
912	NGC 4413, UGC 7538	C	12 26 32.2	12 36 40	3.6	1.7	60 ^f	SBbc	13.0	1.1	2.9	
971	NGC 4423, UGC 7556	P	12 27 09.0	5 52 49	3.8	7.1	18	Sd	14.3	0.5	1.1	
984	NGC 4425, UGC 7562	C	12 27 13.3	12 44 05	3.7	3.0	27	SBa	12.8	< 0.2	< 0.5	
1001 ^f		C	12 27 24.4	13 42 57	0.5	1.5	0	Im	16.6			
1002	NGC 4430, UGC 7566	P	12 27 26.4	6 15 44	2.7	1.1	80	SBc	12.5	1.2	3.2	
1003	NGC 4429, UGC 7568	C	12 27 26.7	11 06 27	10.0	2.3	99	S0/Sa pec	11.4	1.4	4.3	
1043	NGC 4438, UGC 7574	C	12 27 45.6	13 00 32	10.0	2.2	27	Sb (tides)	10.9	3.7	13.1	LINER ^m
1047	NGC 4440, UGC 7581	C	12 27 53.5	12 17 36	2.5	1.2	0	SBa	12.7	< 0.2	< 0.5	
1110	NGC 4450, UGC 7594	P	12 28 29.5	17 05 06	7.6	1.5	175	Sab pec	10.9	1.4	7.6	LINER ⁿ
1121 ^f		C	12 28 41.8	11 07 55	0.9	1.3	0	Im?	16.4			
1158	NGC 4461, UGC 7613	C	12 29 03.0	13 11 02	4.4	2.7	9	Sa	12.1	< 0.2	< 0.8	
1189	IC 3414, UGC 7621	P	12 29 28.9	6 46 12	2.0	1.7	35	Sc	13.7	0.3	0.6	
1196	NGC 4468, UGC 7628	C	12 29 31.1	14 02 58	1.8	1.7	73	S0/a	13.8			
1217	IC 3418, UGC 7630	C	12 29 43.8	11 24 09	2.3	1.5	0	SBm	14.0			
1253	NGC 4477, UGC 7638	C	12 30 02.2	13 38 11	4.5	1.0	15	SB0/SBa	11.3	0.6	1.2	

Table 1—Continued

VCC	Other denomination	C/P ^a	$\alpha(2000.0)$ hh mm ss	$\delta(2000.0)$ ° ' "	D ^b '	R ^c	PA ^d deg	type	B _T mag	F60 ^e Jy	F100 Jy	notes
1326	NGC 4491, UGC 7657	C	12 30 57.2	11 28 59	2.1	2.0	148	SBa	13.4	2.8	3.3	
1368	NGC 4497, UGC 7665	C	12 31 32.5	11 37 29	2.5	2.3	65	SB0/SBa	13.3	< 0.2	< 0.8	
1379	NGC 4498, UGC 7669	P	12 31 39.5	16 51 10	3.5	1.9	133	SBc	12.6	1.1	4.0	
1410	NGC 4502, UGC 7677	P	12 32 03.3	16 41 16	1.3	1.9	0	Sm	14.6	0.2	0.6	
1412	NGC 4503, UGC 7680	C	12 32 06.1	11 10 35	5.4	2.5	12	Sa	12.1	< 0.2	< 1.0	
1419	NGC 4506, UGC 7682	C	12 32 10.5	13 25 11	2.7	1.7	110	S pec (dust)	13.6	< 0.2	< 0.8	
1450	IC 3476, UGC 7695	C	12 32 41.9	14 03 00	3.2	1.3	30	Sc	13.3	1.4	3.1	
1552	NGC 4531, UGC 7729	C	12 34 15.9	13 04 32	5.2	1.7	155	Sa pec	12.6	0.3	1.4	
1554	NGC 4532, UGC 7726	P	12 34 19.3	6 28 07	3.2	2.6	160	Sm	12.3	9.6	16.4	
1569	IC 3520	C	12 34 31.7	13 30 14	1.3	1.5	0	Scd:	15.0			
1575	IC 3521, UGC 7736	P	12 34 39.5	7 09 36	1.3	1.4	0	SBm pec	14.0	1.2	2.3	
1581	UGC 7739	P	12 34 45.3	6 18 02	1.3	1.3	0	Sm	14.5			
1673	NGC 4567, UGC 7777	C	12 36 32.7	11 15 28	3.6	1.5	85	Sc	12.1	20.4	56.8	paired ^P
1675		P	12 36 34.9	8 03 16	1.0	1.7	0	pec	14.5			
1676	NGC 4568, UGC 7776	C	12 36 34.3	11 14 17	6.3	2.9	23	Sc	11.7	20.4	56.8	paired ^P
1678	IC 3576, UGC 7781	P	12 36 37.6	6 37 17	2.7	1.1	0	SBd	13.7	< 0.2	< 0.5	HII
1686	IC 3583, UGC 7784	C	12 36 43.5	13 15 34	3.5	1.6	0	Sm	13.9	0.4	< 1.2	
1690	M 90, NGC 4569, UGC 7786	C	12 36 49.8	13 09 46	13.2	2.0	23	Sab	10.2	8.3	25.0	LINER, Sy ^{1,m,o}
1699	IC 3591, UGC 7790	P	12 37 03.0	6 55 36	1.4	1.9	0	SBm	14.1	< 0.4	< 0.6	
1725		P	12 37 41.2	8 33 33	1.4	1.6	0	Sm/BCD	14.5			
1726	UGC 7795	P	12 37 45.2	7 06 12	1.6	1.3	0	Sdm	14.5			
1727	M 58, NGC 4579, UGC 7796	C	12 37 43.4	11 49 05	7.8	1.3	95	Sab	10.6	4.9	19.6	LINER, Sy1.9 ^{m,o}
1730	NGC 4580, UGC 7794	P	12 37 48.6	5 22 07	2.7	1.3	165	Sc/Sa	12.6	1.3	4.3	
1750		P	12 38 15.5	6 59 39	0.2	2.0	0	BCD	16.5			
1757	NGC 4584, UGC 7803	C	12 38 17.9	13 06 36	2.3	1.9	5	Sa pec	13.7	0.2	0.4	

^asubsample classification: “C” and “P” denote core and periphery, respectively;

^bmajor diameter (in arcmin) to the faintest detectable surface brightness level of approximately 25.5 B-mag arcsec⁻² (VCC); ^cmajor-to-minor axis ratio (VCC);

^dposition angle (PA) of major axis (in degrees, Eastwards from North), taken from the UGC (Nilson 1973), only given where known for VCC galaxies brighter than or equal to $B_T = 14.5$. Face-on galaxies and all galaxies fainter than $B_T = 14.5$ are assigned a value of 0; no galaxy fainter than $B_T = 14.5$ is larger than 3.5 arcmin in major axis diameter - the UGC limit.

^eIRAS 60 μ m spatially integrated flux density (where known), or its upper limit (3σ value). Values are taken from Klatt (1993) for galaxies brighter than $B_T = 14.0$, and from Helou et al. (1988), Moshir et al. (1990), or Thuan & Sauvage (1992) for galaxies fainter than this. ^fgalaxy outside the statistical sample;

^gRauscher 1995; ^hBarth et al. 1998; ⁱPhillips & Malin 1982; ^jPhillips, Charles & Baldwin 1983; ^kFalcke, Wilson & Simpson 1998;

^lKeel 1983; ^mHo, Filippenko & Sargent 1997; ⁿDelgado et al. 1997; ^oStauffer 1982;

^PVCC 1673 is paired with VCC 1676; the integrated IRAS flux density for the pair is given.

^rThe value of 0 degrees for the PA of VCC 912 in the VCC catalog is incorrect. We measured it from an R band image taken at the Calar Alto 2.2-m telescope to be 60 degrees. Our measurement was kindly confirmed by B. Binggeli (private communication).

Table 2. Log-book of the observations

VCC	TDT ^a	filter	raster ^b N _Y × N _Z	α(2000.0) hh mm ss	δ(2000.0) ° ′ ″	θ ^c deg	T _{int} ^d s
1	22500605	C60	2×3	12 08 20.02	13 41 00.2	21.42	864
	22500605	C100	2×3	12 08 20.02	13 41 00.2	21.42	864
	22500606	C160	3×2	12 08 20.02	13 41 00.2	21.39	328
17	22500607	C60	2×3	12 10 01.87	14 21 42.5	21.36	864
	22500607	C100	2×3	12 10 01.87	14 21 42.5	21.45	864
	22500608	C160	3×2	12 10 01.87	14 21 42.5	21.35	328
24	23501521	C60	2×3	12 10 36.15	11 45 36.6	19.77	864
	23501521	C100	2×3	12 10 36.15	11 45 36.6	19.69	864
	23501522	C160	3×2	12 10 36.15	11 45 36.6	19.76	328
66	23501529	C60	6×1	12 12 46.87	10 52 06.9	20.07	820
	23501529	C100	6×1	12 12 46.87	10 52 06.9	20.10	820
	23501530	C160	6×1	12 12 46.87	10 52 07.0	20.09	328
81	22500609	C60	2×3	12 13 26.18	14 46 19.3	21.36	864
	22500609	C100	2×3	12 13 26.18	14 46 19.2	21.32	864
	22500610	C160	4×2	12 13 26.18	14 46 19.3	21.41	378
87	22500611	C60	2×3	12 13 40.52	15 27 13.2	21.33	864
	22500611	C100	2×3	12 13 40.52	15 27 13.2	21.43	864
	22500612	C160	4×2	12 13 40.52	15 27 13.2	21.27	378
92	22500619	C60	6×1	12 13 48.34	14 54 07.1	21.42	820
	22500619	C100	6×1	12 13 48.34	14 54 07.0	21.43	820
	22500620	C160	6×1	12 13 48.34	14 54 07.1	21.40	304
130	22500443	C60	2×3	12 15 04.23	09 45 13.6	22.31	1056
	22500443	C100	2×3	12 15 04.23	09 45 13.6	22.23	1056
	22500444	C160	3×2	12 15 04.23	09 45 13.6	22.27	424
152	22500445	C60	3×1	12 15 31.21	09 35 07.6	22.28	768
	22500445	C100	3×1	12 15 31.21	09 35 07.6	22.30	768
	22500446	C160	3×2	12 15 31.21	09 35 07.7	22.31	328
159	22500433	C60	2×3	12 15 41.50	08 17 07.7	22.47	864
	22500433	C100	2×3	12 15 41.50	08 17 07.7	22.53	864
	22500434	C160	3×2	12 15 41.50	08 17 07.7	22.46	328
169	22500441	C60	2×3	12 15 56.39	09 38 55.8	22.28	1056
	22500441	C100	2×3	12 15 56.39	09 38 55.8	22.28	1056
	22500442	C160	3×2	12 15 56.39	09 38 55.8	22.32	424
318	22500439	C60	2×3	12 19 02.91	08 51 26.8	22.45	864
	22500439	C100	2×3	12 19 02.91	08 51 26.8	22.46	864
	22500440	C160	3×2	12 19 02.91	08 51 26.9	22.46	328
459	23402367	C60	2×3	12 21 11.46	17 38 15.5	18.54	864
	23402367	C100	2×3	12 23 37.65	17 32 28.5	18.69	864
	23402368	C160	3×2	12 21 11.46	17 38 15.5	18.49	328
460	23402369	C60	5×1	12 21 13.18	18 23 03.4	18.29	781
	23402369	C100	5×1	12 21 13.18	18 23 03.3	18.29	781
	23402370	C160	5×1	12 21 13.18	18 23 03.4	18.29	283
655	23402365	C60	3×1	12 23 37.65	17 32 28.5	18.69	768
	23402365	C100	3×1	12 23 37.65	17 32 28.5	18.68	768
	23402366	C160	4×2	12 23 37.65	17 32 28.5	18.67	378
664	22500181	C60	3×2	12 23 44.26	12 28 40.6	22.32	967
	22500181	C100	3×2	12 23 44.26	12 28 40.6	22.30	967
	22500182	C160	4×2	12 23 44.26	12 28 40.7	22.32	378
666	23402359	C60	2×3	12 23 46.13	16 47 28.6	18.96	1056
	23402359	C100	2×3	12 23 46.13	16 47 28.6	18.88	1056
	23402360	C160	3×2	12 23 46.13	16 47 28.6	18.91	424

Table 2—Continued

VCC	TDT ^a	filter	raster ^b N _Y × N _Z	α(2000.0) hh mm ss	δ(2000.0) ° ′ ″	θ ^c deg	T _{int} ^d s
692	22500179	C60	4×1	12 24 01.68	12 12 16.6	22.37	806
	22500179	C100	4×1	12 24 01.68	12 12 16.7	22.38	806
	22500180	C160	3×2	12 24 01.68	12 12 16.8	30.65	328
836	22500183	C60	4×1	12 25 45.91	12 39 41.5	22.40	806
	22500183	C100	4×1	12 25 45.91	12 39 41.5	22.40	806
	22500184	C160	5×1	12 25 45.91	12 39 41.4	22.41	283
848	22500207	C60	2×3	12 25 52.78	05 48 29.5	22.92	864
	22500207	C100	2×3	12 25 52.78	05 48 29.5	22.90	864
	22500208	C160	4×2	12 25 52.78	05 48 29.5	22.96	378
857	23402363	C60	5×1	12 25 55.94	18 12 47.4	18.62	821
	23402363	C100	5×1	12 25 55.94	18 12 47.4	18.64	821
	23402364	C160	6×1	12 25 55.94	18 12 47.4	18.63	328
873	22500191	C60	3×1	12 26 06.82	13 06 47.5	22.37	768
	22500191	C100	3×1	12 26 06.82	13 06 47.5	22.37	768
	22500192	C160	5×1	12 26 06.81	13 06 47.4	22.35	283
890	22500205	C60	2×3	12 26 20.86	06 40 05.7	22.87	864
	22500205	C100	2×3	12 26 20.86	06 40 05.7	22.95	864
	22500206	C160	3×2	12 26 20.86	06 40 05.7	22.92	328
912	22500185	C60	4×1	12 26 32.06	12 36 41.7	22.42	806
	22500185	C100	4×1	12 26 32.06	12 36 41.7	22.43	806
	22500186	C160	4×1	12 26 32.06	12 36 41.7	22.43	278
971	22500209	C60	4×1	12 27 09.53	05 52 48.1	22.96	806
	22500209	C100	4×1	12 27 09.53	05 52 48.0	22.98	806
	22500210	C160	3×1	12 27 09.53	05 52 48.0	22.92	253
984	22500187	C60	3×2	12 27 14.00	12 44 06.3	22.44	967
	22500187	C100	3×2	12 27 14.00	12 44 06.2	22.45	967
	22500188	C160	3×1	12 27 14.00	12 44 06.1	22.43	253
1001	61300103	C100	2×3	12 27 24.65	13 43 00.3	16.30	1104
	61300104	C160	3×2	12 27 24.65	13 43 00.3	16.33	668
1002	22500217	C60	4×1	12 27 26.27	06 15 42.3	22.94	806
	22500217	C100	4×1	12 27 26.27	06 15 42.2	22.94	806
	22500218	C160	4×1	12 27 26.27	06 15 42.2	22.96	278
1003	22500175	C60	5×1	12 27 26.21	11 06 30.1	22.61	781
	22500175	C100	5×1	12 27 26.21	11 06 30.3	22.62	781
	22500176	C160	5×1	12 27 26.20	11 06 30.2	22.61	303
1043	22500189	C60	10×1	12 27 45.72	13 00 30.3	22.45	976
	22500189	C100	10×1	12 27 45.72	13 00 30.3	22.44	976
	22500190	C160	9×1	12 27 45.72	13 00 30.3	22.43	367
1047	22500173	C60	2×3	12 27 53.62	12 17 36.5	22.53	864
	22500173	C100	2×3	12 27 53.62	12 17 36.5	22.49	864
	22500174	C160	3×1	12 27 53.62	12 17 36.4	22.50	253
1110	23402371	C60	6×1	12 28 29.47	17 05 06.8	19.07	1168 ^{†e}
	23402371	C100	6×1	12 28 29.47	17 05 06.7	19.03	1168 [†]
	23402372	C160	5×1	12 28 29.47	17 05 06.7	19.05	897 [†]
1121	61600117	C100	2×3	12 28 41.77	11 07 54.8	16.73	1104
	61600118	C160	3×2	12 28 41.74	11 07 54.9	16.74	668
1158	19900549	C60	4×2	12 29 03.01	13 11 07.2	28.97	983 [†]
	19900549	C100	4×2	12 29 03.01	13 11 07.1	28.96	983 [†]
	19900550	C160	4×1	12 29 03.00	13 11 07.0	28.96	278 [†]
1189	22500201	C60	2×3	12 29 28.53	06 46 19.3	22.99	864
	22500201	C100	2×3	12 29 28.53	06 46 19.3	22.95	864

Table 2—Continued

VCC	TDT ^a	filter	raster ^b N _Y × N _Z	α(2000.0) hh mm ss	δ(2000.0) ° ' "	θ ^c deg	T _{int} ^d s	
		22500202	C160	4×2	12 29 28.53	06 46 19.3	22.98	378
1196		19900545	C60	2×3	12 29 31.05	14 02 55.3	29.29	864 [†]
		19900545	C100	2×3	12 29 31.05	14 02 55.3	29.25	864 [†]
		19900546	C160	3×2	12 29 31.05	14 02 55.3	29.25	328 [†]
1217		22500177	C60	2×3	12 29 43.44	11 24 07.5	22.78	864
		22500177	C100	2×3	12 29 43.44	11 24 07.4	22.84	864
		22500178	C160	4×2	12 29 43.44	11 24 07.5	22.70	378
1253		19900547	C60	5×1	12 30 02.87	13 38 07.5	29.20	821 [†]
		19900547	C100	5×1	12 30 02.87	13 38 07.5	29.19	821 [†]
		19900548	C160	5×1	12 30 02.86	13 38 07.5	29.17	328 [†]
1326		22500335	C60	3×1	12 30 57.15	11 29 02.0	22.66	768
		22500335	C100	3×1	12 30 57.15	11 29 02.0	22.66	768
		22500336	C160	3×1	12 30 57.15	11 29 02.0	22.66	253
1368		22500333	C60	2×3	12 31 32.49	11 37 26.5	22.62	864
		22500333	C100	2×3	12 31 32.49	11 37 26.5	22.60	864
		22500334	C160	4×1	12 31 32.49	11 37 26.4	22.69	278
1379		23402683	C60	3×1	12 31 39.43	16 51 14.5	19.26	768
		23402683	C100	3×1	12 31 39.43	16 51 14.4	19.27	768
		23402684	C160	3×1	12 31 39.43	16 51 14.4	19.26	253
1410		23402681	C60	2×3	12 32 03.42	16 41 14.8	19.33	864
		23402681	C100	2×3	12 32 03.42	16 41 14.8	19.36	864
		23402682	C160	3×2	12 32 03.42	16 41 14.8	19.32	328
1412		22500331	C60	5×1	12 32 05.53	11 10 38.7	22.73	821
		22500331	C100	5×1	12 32 05.53	11 10 38.7	22.73	821
		22500332	C160	6×1	12 32 05.53	11 10 38.7	22.75	328
1419		19900551	C60	2×2	12 32 10.56	13 25 14.8	29.38	839 [†]
		19900551	C100	2×2	12 32 10.56	13 25 14.8	29.35	839 [†]
		19900552	C160	4×1	12 32 10.56	13 25 14.7	29.35	278 [†]
1450		19900561	C60	3×1	12 32 42.21	14 02 57.1	29.50	768 [†]
		19900561	C100	3×1	12 32 42.21	14 02 57.2	29.55	768 [†]
		19900562	C160	5×1	12 32 42.21	14 02 57.1	29.56	303 [†]
1552		19900553	C60	4×1	12 34 15.87	13 04 34.0	29.43	806 [†]
		19900553	C100	4×1	12 34 15.87	13 04 34.0	29.43	806 [†]
		22600876	C160	5×1	12 34 15.86	13 04 34.0	22.42	303 [†]
1554		22500213	C60	3×1	12 34 19.41	06 28 10.1	23.05	768
		22500213	C100	3×1	12 34 19.41	06 28 10.1	23.08	768
		22500214	C160	4×1	12 34 19.41	06 28 10.0	23.09	262
1569		19900543	C60	2×3	12 34 31.38	13 30 22.3	29.64	864 [†]
		19900543	C100	2×3	12 34 31.38	13 30 22.3	29.56	864 [†]
		19900544	C160	3×2	12 34 31.38	13 30 22.3	29.60	328 [†]
1575		22500215	C60	3×1	12 34 39.08	07 09 40.4	23.08	768
		22500215	C100	3×1	12 34 39.08	07 09 40.4	23.08	768
		22500216	C160	3×1	12 34 39.08	07 09 40.3	23.08	253
1581		22500211	C60	2×3	12 34 44.63	06 18 10.4	23.10	864
		22500211	C100	2×3	12 34 44.63	06 18 10.4	23.15	864
		22500212	C160	3×2	12 34 44.63	06 18 10.4	23.12	328
1673/1676		22500325	C60	4×5	12 36 33.46	11 14 56.6	22.88	1422
		22500325	C100	4×5	12 36 33.46	11 14 56.6	22.94	1422
		22500326	C160	8×3	12 36 33.46	11 14 56.6	22.93	682
1675		22802737	C60	2×3	12 36 34.65	08 03 17.6	22.57	864
		22802737	C100	2×3	12 36 34.65	08 03 17.6	22.59	864

Table 2—Continued

VCC	TDT ^a	filter	raster ^b N _Y × N _Z	α(2000.0) hh mm ss	δ(2000.0) ° ′ ″	θ ^c deg	T _{int} ^d s
	22802738	C160	3×2	12 36 34.65	08 03 17.6	22.49	328
1678	22500513	C60	3×2	12 36 37.31	06 37 17.6	23.13	967
	22500513	C100	3×2	12 36 37.31	06 37 17.6	23.10	967
	22500514	C160	4×1	12 36 37.30	06 37 17.5	23.10	278
1686	19900557	C60	3×3	12 36 43.87	13 15 29.7	29.73	1164 [†]
	19900557	C100	3×3	12 36 43.87	13 15 29.7	15.33	1164 [†]
	19900558	C160	5×1	12 36 43.87	13 15 29.6	29.70	303 [†]
1690	19900559	C60	12×1	12 36 49.88	13 09 53.7	29.69	1054 [†]
	19900559	C100	12×1	12 36 49.88	13 09 53.7	29.68	1054 [†]
	19900560	C160	10×1	12 36 49.88	13 09 53.6	29.69	388 [†]
1699	22500511	C60	2×3	12 37 02.43	06 55 47.9	23.07	864
	22500511	C100	2×3	12 37 02.44	06 55 47.9	23.08	864
	22500512	C160	4×2	12 37 02.44	06 55 47.9	23.09	378
1725	22802735	C60	2×3	12 37 41.11	08 33 30.4	22.48	864
	22802735	C100	2×3	12 37 41.11	08 33 30.4	22.44	864
	22802736	C160	4×2	12 37 41.11	08 33 30.5	22.48	378
1726	22500509	C60	2×3	12 37 44.38	07 06 12.4	23.20	864
	22500509	C100	2×3	12 37 44.38	07 06 12.4	23.20	864
	22500510	C160	4×2	12 37 44.38	07 06 12.4	23.12	378
1727	22500329	C60	5×1	12 37 43.47	11 49 06.3	22.95	781
	22500329	C100	5×1	12 37 43.48	11 49 06.3	22.95	781
	22500330	C160	6×1	12 37 43.48	11 49 06.2	22.95	304
1730	22500521	C60	2×2	12 37 48.90	05 22 06.5	23.16	839
	22500521	C100	2×2	12 37 48.90	05 22 06.5	23.15	839
	22500522	C160	4×2	12 37 48.90	05 22 06.5	23.16	378
1750	22500507	C60	2×3	12 38 14.98	06 59 42.8	23.18	1056
	22500507	C100	2×3	12 38 14.98	06 59 42.8	23.11	1056
	22500508	C160	3×2	12 38 14.98	06 59 42.8	23.15	424
1757	22600875	C60	2×3	12 38 17.99	13 06 36.8	22.59	864 [†]
	22600875	C100	2×3	12 38 17.99	13 06 36.8	22.67	864 [†]
	19900556	C160	4×2	12 38 17.99	13 06 36.8	29.83	378 [†]

^aTarget Dedicated Time (TDT) identifier;

^braster pointing pattern (in spacecraft Y and Z);

^cposition angle (θ) of the spacecraft Y axis (positive East from North);

^don-target integration time (T_{int});

^e† indicates repeated observation.

Table 4. The Fitting Parameters

VCC	λ μm	One Gaussian Fit			Two Gaussian Fit				χ^2	comments	
		S $\frac{\text{MJy}}{\text{sr}}$	$\epsilon(\text{S})$ $\frac{\text{MJy}}{\text{sr}}$	σ^1 "	S_n^2 $\frac{\text{MJy}}{\text{sr}}$	$\epsilon(S_n)$ $\frac{\text{MJy}}{\text{sr}}$	S_d^3 $\frac{\text{MJy}}{\text{sr}}$	$\epsilon(S_d)$ $\frac{\text{MJy}}{\text{sr}}$			σ_d^4 "
1	60	2.05	0.33	4.38	0.70	
	100	2.39	0.31	9.87	0.52	
	170	0.79	0.11	52.19	0.59	
17	60	0.85	0.29	0.79	beam fit; non-detection
	100	0.21	0.27	0.47	beam fit; non-detection
	170	0.01	0.10	0.40	beam fit; non-detection
24	60	0.68	0.31	0.59	beam fit; non-detection
	100	0.79	0.29	0.25	beam fit; non-detection
	170	0.47	0.13	0.09	0.24	
66	60	multi-component fit ⁵
	100	multi-component fit ⁵
	170	20.76	0.21	68.58	3.10	
81	60	0.26	0.27	0.57	beam fit; non-detection
	100	0.18	0.24	0.33	beam fit; non-detection
	170	1.12	0.09	59.96	0.70	
87	60	1.97	0.47	0.86	beam fit
	100	2.82	0.46	0.47	beam fit
	170	1.46	0.09	0.02	1.58	
92	60	57.05	2.12	9.43	1.26	53.53	0.21	
	100	65.93	3.76	27.46	1.12	72.67	0.90	
	170	42.39	0.53	117.29	0.20	
130	60	-0.42	0.34	0.54	beam fit; non-detection
	100	1.23	0.32	0.07	0.28	
	170	0.31	0.08	5.26	0.31	
152	60	28.41	1.15	14.41	0.21	
	100	78.35	2.07	2.62	0.55	80.90	0.02	
	170	20.58	0.33	1.92	0.24	135.66	0.40	
159	60	0.22	0.27	0.43	beam fit; non-detection
	100	0.11	0.27	0.29	beam fit; non-detection
	170	0.60	0.10	0.76	beam fit ⁶
169	60	0.32	0.19	0.63	beam fit; non-detection
	100	-0.13	0.34	0.34	beam fit; non-detection
	170	-0.02	0.07	0.66	beam fit; non-detection
318	60	2.84	0.31	0.01	0.65	
	100	3.02	0.29	27.29	0.16	
	170	2.60	0.12	33.87	0.53	
459	60	2.12	0.35	13.49	0.87	
	100	5.18	0.36	17.17	0.44	
	170	1.95	0.13	6.05	0.27	
460	60	62.62	1.71	11.41	0.72	modified beam ⁷
	100	121.00	4.06	8.51	0.53	77.18	0.20	modified beam ⁷
	170	26.08	1.92	5.49	1.23	78.65	0.18	
655	60	7.51	0.58	5.34	0.49	
	100	16.66	0.63	9.18	0.25	
	170	18.57	0.12	13.59	1.59	
664	60	6.14	0.76	1.31	0.43	52.38	0.88	
	100	5.90	0.93	2.67	0.72	34.38	0.76	
	170	3.75	0.10	0.01	0.78	
666	60	-0.50	0.20	1.08	beam fit; non-detection

Table 4—Continued

VCC	λ μm	One Gaussian Fit			Two Gaussian Fit				σ_d^4 "	χ^2	comments
		S $\frac{\text{MJy}}{\text{sr}}$	$\epsilon(\text{S})$ $\frac{\text{MJy}}{\text{sr}}$	σ^1 "	S_n^2 $\frac{\text{MJy}}{\text{sr}}$	$\epsilon(S_n)$ $\frac{\text{MJy}}{\text{sr}}$	S_d^3 $\frac{\text{MJy}}{\text{sr}}$	$\epsilon(S_d)$ $\frac{\text{MJy}}{\text{sr}}$			
	100	0.35	0.20	0.41	beam fit; non-detection
	170	-0.10	0.06	0.55	beam fit; non-detection
692	60	7.11	0.51	15.56	0.81	
	100	13.70	1.29	3.45	1.00	39.81	0.78	
	170	7.54	0.20	0.82	0.14	144.89	2.13	
836	60	86.91	5.07	38.71	3.57	32.21	0.89	modified beam ⁷
	100	204.30	8.46	78.11	4.57	32.64	0.63	modified beam ⁷
	170	40.72	0.74	25.63	1.29	
848	60	0.45	0.27	0.64	beam fit; non-detection
	100	0.81	0.25	0.05	0.30	
	170	0.75	0.16	0.48	0.10	137.07	0.44	
857	60	5.99	0.48	20.77	0.59	
	100	6.07	1.25	9.26	0.58	41.14	1.43	modified beam ⁷
	170	14.83	0.35	42.38	0.20	
873	60	32.98	0.73	34.57	1.00	
	100	poor fit
	170	49.50	0.80	41.03	1.92	
890	60	0.40	0.27	0.62	beam fit; non-detection
	100	0.38	0.24	0.41	beam fit; non-detection
	170	0.37	0.12	18.77	0.28	
912	60	12.14	0.61	13.66	1.19	
	100	18.34	2.15	8.87	1.67	34.65	0.62	
	170	10.04	0.34	22.81	0.22	
971	60	4.53	0.39	17.38	0.67	
	100	10.62	0.46	24.39	0.60	
	170	4.29	0.29	33.38	0.14	
984	60	0.06	0.30	0.52	beam fit; non-detection
	100	0.20	0.32	0.28	beam fit; non-detection
	170	-0.15	0.24	0.23	beam fit; non-detection
1001	60	not observed
	100	-0.05	0.14	0.69	beam fit; non-detection
	170	0.52	0.06	42.32	0.73	
1002	60	10.72	0.52	17.78	0.81	
	100	16.78	1.45	11.98	0.87	34.65	0.65	
	170	14.84	0.31	30.67	0.27	
1003	60	16.25	0.84	5.58	0.91	
	100	43.84	1.44	1.98	0.38	108.49	0.20	
	170	12.37	0.24	0.01	0.54	
1043	60	43.04	1.41	5.78	0.60	
	100	89.99	3.09	7.17	0.78	71.48	0.20	
	170	34.40	0.57	2.83	0.21	188.97	0.20	
1047	60	0.33	0.28	0.84	beam fit; non-detection
	100	-0.03	0.27	0.48	beam fit; non-detection
	170	-0.31	0.31	0.22	beam fit; non-detection
1110	60	5.72	0.85	2.56	0.41	73.70	0.54	
	100	9.19	1.70	15.77	1.11	42.75	0.20	
	170	18.19	0.30	56.06	0.20	
1121	60	not observed
	100	0.33	0.18	0.26	beam fit; non-detection

Table 4—Continued

VCC	λ μm	One Gaussian Fit			Two Gaussian Fit			$\epsilon(S_d)$ $\frac{\text{MJy}}{\text{sr}}$	σ_d^4 "	χ^2	comments
		S $\frac{\text{MJy}}{\text{sr}}$	$\epsilon(S)$ $\frac{\text{MJy}}{\text{sr}}$	σ^1 "	S_n^2 $\frac{\text{MJy}}{\text{sr}}$	$\epsilon(S_n)$ $\frac{\text{MJy}}{\text{sr}}$	S_d^3 $\frac{\text{MJy}}{\text{sr}}$				
	170	confusion limited
1158	60	-0.25	0.31	0.65	...	beam fit; non-detection
	100	0.21	0.34	0.32	...	beam fit; non-detection
	170	-0.60	0.20	0.42	...	beam fit; non-detection
1189	60	2.53	0.31	16.24	0.97	...	
	100	5.93	0.27	18.64	0.77	...	
	170	4.20	0.12	11.22	0.63	...	
1196	60	-0.19	0.30	0.33	...	beam fit; non-detection
	100	0.20	0.28	0.19	...	beam fit; non-detection
	170	poor fit ⁸
1217	60	-0.03	0.30	0.51	...	beam fit; non-detection
	100	0.08	0.26	0.34	...	beam fit; non-detection
	170	-0.15	0.09	1.49	...	beam fit; non-detection
1253	60	2.60	0.85	0.62	...	
	100	9.79	1.07	14.10	0.35	...	
	170	3.66	0.29	19.29	0.43	...	
1326	60	34.83	1.30	1.97	0.62	56.51	1.21	
	100	36.85	0.91	1.29	0.18	95.09	0.39	
	170	6.35	0.65	23.84	0.68	...	
1368	60	-0.39	1.14	1.14	...	beam fit; non-detection
	100	0.41	0.19	0.61	...	beam fit; non-detection
	170	0.87	0.21	0.85	...	beam fit
1379	60	6.95	0.39	37.76	1.93	...	
	100	9.52	1.01	10.59	0.69	51.71	5.84	
	170	13.20	0.41	39.05	0.87	...	
1410	60	2.25	0.22	25.45	1.12	...	
	100	6.18	0.43	7.63	0.73	...	
	170	2.56	0.13	13.24	0.52	...	
1412	60	-0.36	0.44	0.93	...	beam fit; non-detection
	100	-0.37	0.53	1.11	...	beam fit; non-detection
	170	2.41	0.27	27.95	1.44	...	off-center emission
1419	60	1.17	0.36	0.39	0.64	...	
	100	3.23	0.42	19.24	0.53	...	
	170	1.60	0.26	8.85	1.31	...	
1450	60	8.72	0.64	18.28	0.84	...	
	100	23.49	1.64	7.86	0.96	39.35	1.31	
	170	11.18	0.37	30.00	0.23	...	
1552	60	4.52	1.28	15.31	0.51	...	modified beam ⁷
	100	15.53	0.80	19.70	0.95	...	modified beam ⁷
	170	6.44	0.42	21.34	0.45	...	
1554	60	multi-component fit ⁵
	100	multi-component fit ⁵
	170	34.24	0.60	28.55	0.52	...	
1569	60	0.66	0.37	0.35	...	beam fit; non-detection
	100	0.39	0.34	0.31	...	beam fit; non-detection
	170	0.26	0.09	0.30	...	beam fit; non-detection
1575	60	17.17	0.71	11.39	1.25	...	
	100	24.42	2.32	5.54	1.71	29.78	0.75	
	170	8.40	0.43	25.17	0.33	...	

Table 4—Continued

VCC	λ μm	One Gaussian Fit			Two Gaussian Fit			$\epsilon(S_d)$ $\frac{\text{MJy}}{\text{sr}}$	σ_d^4 "	χ^2	comments
		S $\frac{\text{MJy}}{\text{sr}}$	$\epsilon(S)$ $\frac{\text{MJy}}{\text{sr}}$	σ^1 "	S_n^2 $\frac{\text{MJy}}{\text{sr}}$	$\epsilon(S_n)$ $\frac{\text{MJy}}{\text{sr}}$	S_d^3 $\frac{\text{MJy}}{\text{sr}}$				
1581	60	0.14	0.24	0.88	beam fit; non-detection
	100	0.58	0.22	0.59	beam fit; non-detection
	170	1.22	0.24	7.69	0.31	
1673	60	
	100	
	170	multi-component fit ⁵
1675	60	0.80	0.25	14.40	0.74	
	100	-0.08	0.24	0.41	beam fit; non-detection
	170	0.60	0.14	6.73	0.20	
1678	60	1.59	0.32	0.84	beam fit
	100	2.04	0.26	35.11	0.37	
	170	1.76	0.30	33.78	0.27	
1686	60	7.86	1.18	7.09	0.93	
	100	10.74	0.55	23.35	0.78	
	170	5.72	0.38	17.39	0.81	
1690	60	68.43	2.85	8.36	1.21	60.01	0.60	
	100	86.07	5.08	32.24	1.73	63.74	3.79	
	170	59.57	0.65	54.95	0.20	
1699	60	5.14	0.14	6.26	0.78	
	100	5.28	0.32	16.19	0.50	
	170	1.89	0.10	0.03	0.44	
1725	60	0.93	0.31	0.57	beam fit
	100	5.11	0.81	6.38	0.36	
	170	1.88	0.11	0.03	0.41	
1726	60	0.68	0.35	0.49	beam fit; non-detection
	100	0.74	0.38	0.38	beam fit; non-detection
	170	0.94	0.10	0.03	0.38	
1727	60	21.36	1.49	11.67	0.77	55.87	2.32	
	100	multi-component fit ⁵
	170	8.32	1.48	33.81	1.07	84.61	0.20	
1730	60	14.69	2.25	7.18	1.53	28.46	0.46	modified beam ⁷
	100	31.35	3.19	21.69	2.06	27.14	0.48	modified beam ⁷
	170	16.79	0.97	1.86	0.89	52.01	0.76	
1750	60	0.17	0.22	0.66	beam fit; non-detection
	100	0.71	0.22	11.41	0.42	
	170	0.29	0.08	0.44	0.19	
1757	60	1.89	0.23	3.87	1.69	
	100	6.71	0.24	18.38	0.99	
	170	3.27	0.13	11.38	0.29	

¹The width σ of the major axis of the elliptical Gaussian source model in arcsec, where the total width of the major axis of the fitted Gaussian is $\sigma_{\text{total}}^2 = \sigma^2 + \sigma_{\text{PSF}}^2$. The FWHM of the source model is 2.354σ ;

²The amplitude S_n of the nuclear component; ³ The amplitude S_d of the disk component;

⁴The width σ_d of the disk major axis in arcsec, where the total width of the major axis of the fitted Gaussian for the disk component is $\sigma_{\text{total}}^2 = \sigma_d^2 + \sigma_{\text{PSF}}^2$;

⁵The parameters for the multi-component fit are listed in Tables 5,6.

⁶VCC 159 shows evidence for faint extended emission at $160\mu\text{m}$, not fitted by the model. We only present a beam fit to the data, resulting in a lower limit for the derived flux.

⁷In some cases it was necessary to consider a narrower width for the beam fit model, namely $\sigma = 15.41''$, FWHM = $2.355 \times \sigma$ (see Sect. 6.2.1).

⁸VCC 1196 presents evidence for extended asymmetric emission, not fitted by the model. In this case the fluxes were derived only from the integration of the raw maps.

Table 5. The Fitting Parameters for the multi-component fits

VCC	λ μm	Main nuclear/disk component					Other components			χ^2	comments
		$S1_n^1$ $\frac{\text{MJy}}{\text{sr}}$	$\epsilon(S1_n)$ $\frac{\text{MJy}}{\text{sr}}$	$S1_d^2$ $\frac{\text{MJy}}{\text{sr}}$	$\epsilon(S1_d)$ $\frac{\text{MJy}}{\text{sr}}$	$\sigma1_d^3$ "	S2 $\frac{\text{MJy}}{\text{sr}}$	$\epsilon(S2)$ $\frac{\text{MJy}}{\text{sr}}$	$\sigma2$ "		
66	60	8.33	1.35	7.60	0.91	52.40	8.55	0.76	4.63	1.12	
	100	11.47	1.95	18.21	1.11	56.23	5.49	0.91	...	2.21	
1554	60	54.22	2.22	10.50	1.10	31.23	24.81	1.64	18.60	4.36	modified beam ⁴
	100	29.57	2.87	27.61	1.51	35.04	28.59	1.72	25.29	10.21	modified beam ⁴
1727	100	17.78	4.92	29.78	1.26	43.51	14.61	0.72	59.42	0.15	modified beam ⁴

¹The amplitude $S1_n$ of the nuclear component;

²The amplitude $S1_d$ of the disk component;

³The width $\sigma1_d$ of the disk major axis in arcsec, where the total width of the major axis of the fitted Gaussian for the disk component is $\sigma1_{\text{total}}^2 = \sigma1_d^2 + \sigma_{\text{PSF}}^2$;

⁴In some cases it was necessary to consider a narrower beam for the fit, namely a spherical Gaussian with the width $\sigma = 15.41''$, $\text{FWHM} = 2.355 \times \sigma$ (see Sect. 6.2.1).

Table 6. The Fitting Parameters for VCC 1673/VCC 1676

λ μm	VCC 1676					VCC 1673					χ^2
	$S1_n$ $\frac{\text{MJy}}{\text{sr}}$	$\epsilon(S1_n)$ $\frac{\text{MJy}}{\text{sr}}$	$S1_d$ $\frac{\text{MJy}}{\text{sr}}$	$\epsilon(S1_d)$ $\frac{\text{MJy}}{\text{sr}}$	$\sigma1_d$ "	$S2_n$ $\frac{\text{MJy}}{\text{sr}}$	$\epsilon(S2_n)$ $\frac{\text{MJy}}{\text{sr}}$	$S2_d$ $\frac{\text{MJy}}{\text{sr}}$	$\epsilon(S2_d)$ $\frac{\text{MJy}}{\text{sr}}$	$\sigma2_d$ "	
170	29.45	2.72	54.52	2.03	52.68	57.08	0.63	9.18	0.10	239.00	0.2

Table 7. The Photometry

VCC	λ μm	F_{model}^1 Jy	$\epsilon(F_{\text{model}})$ Jy	F_{map}^2 Jy	$\epsilon(F_{\text{map}})$ Jy	B_{backgr}^3 $\frac{\text{MJy}}{\text{sr}}$	f_B^4	notes
1	60	0.10	0.02	-0.05	0.06	15.87	0.037	
	100	0.14	0.02	0.21	0.06	8.92	0.042	
	170	0.33	0.05	0.31	0.18	7.46	0.042	
17	60	<0.04	...	0.11	0.08	14.80	0.037	
	100	<0.03	...	-0.09	0.08	9.10	0.033	
	170	<0.07	...	0.01	0.19	7.94	0.036	
24	60	<0.04	...	0.11	0.06	16.77	0.030	
	100	<0.04	...	-0.08	0.06	9.72	0.043	
	170	0.12	0.03	0.04	0.05	5.42	0.020	
66	60	2.47	0.21	2.96	0.30	19.40	0.027	
	100	5.09	0.28	5.32	0.43	11.47	0.039	
	170	11.27	0.03	10.64	0.21	6.02	0.039	
81	60	<0.04	...	0.02	0.06	14.84	0.052	
	100	<0.03	...	0.09	0.07	9.09	0.060	
	170	0.77	0.06	0.90	0.23	7.73	0.038	
87	60	0.10	0.02	0.10	0.08	14.79	0.034	
	100	0.15	0.02	0.26	0.12	8.50	0.038	
	170	0.38	0.02	0.06	0.11	7.69	0.023	
92	60	4.70	0.26	4.64	0.13	16.02	0.036	
	100	11.46	0.38	10.41	0.21	9.86	0.040	
	170	40.29	0.50	26.16	0.41	10.05	0.028	
130	60	<0.05	...	0.19	0.05	17.38	0.030	
	100	0.07	0.02	-0.03	0.05	9.30	0.026	
	170	0.08	0.02	0.00	0.14	5.45	0.042	
152	60	1.87	0.08	1.98	0.09	17.93	0.025	
	100	5.48	0.29	3.88	0.10	11.25	0.043	
	170	8.38	0.38	6.80	0.21	6.06	0.045	
159	60	<0.04	...	-0.00	0.04	16.95	0.023	
	100	<0.04	...	0.02	0.06	9.44	0.021	
	170	0.16	0.03	0.49	0.21	6.12	0.044	
169	60	<0.03	...	-0.14	0.05	16.89	0.021	
	100	<0.05	...	-0.01	0.05	9.55	0.025	
	170	<0.05	...	-0.18	0.14	5.71	0.043	
318	60	0.13	0.01	0.13	0.09	16.82	0.031	
	100	0.35	0.03	0.67	0.11	9.30	0.017	
	170	0.96	0.04	1.07	0.23	5.97	0.049	
459	60	0.13	0.02	0.51	0.06	13.24	0.023	
	100	0.38	0.03	0.79	0.18	7.50	0.037	
	170	0.50	0.03	0.45	0.11	6.59	0.042	
460	60	3.29	0.09	4.05	0.48	14.61	0.041	
	100	9.11	0.33	7.62	0.47	8.98	0.084	
	170	11.25	1.10	9.57	0.28	7.79	0.036	
655	60	0.42	0.03	0.46	0.08	12.64	0.025	
	100	1.11	0.04	1.01	0.06	7.43	0.037	
	170	5.36	0.03	5.41	0.12	5.70	0.045	
664	60	0.75	0.15	0.83	0.14	15.13	0.033	
	100	0.77	0.13	1.12	0.10	8.92	0.020	
	170	0.97	0.03	0.85	0.18	5.16	0.026	
666	60	<0.03	...	0.07	0.05	13.49	0.025	
	100	<0.03	...	0.12	0.06	7.71	0.028	
	170	<0.04	...	0.03	0.09	5.11	0.037	

Table 7—Continued

VCC	λ μm	F_{model}^1 Jy	$\epsilon(F_{\text{model}})$ Jy	F_{map}^2 Jy	$\epsilon(F_{\text{map}})$ Jy	B_{backgr}^3 $\frac{\text{MJy}}{\text{sr}}$	f_B^4	notes
692	60	0.54	0.04	0.56	0.09	14.89	0.035	
	100	1.43	0.21	1.37	0.09	8.65	0.031	
	170	3.91	0.09	3.12	0.28	4.45	0.033	
836	60	7.03	0.38	7.35	0.18	17.62	0.051	
	100	14.22	0.50	14.43	0.26	9.04	0.070	
	170	11.63	0.21	12.18	0.28	6.14	0.015	
848	60	<0.06	...	0.19	0.04	17.61	0.028	
	100	0.05	0.01	0.16	0.03	10.17	0.021	
	170	1.41	0.26	1.06	0.37	6.34	0.044	
857	60	0.65	0.05	0.79	0.13	12.71	0.022	
	100	2.83	0.17	2.72	0.12	7.19	0.037	
	170	7.76	0.18	6.76	0.21	5.24	0.037	
873	60	3.82	0.08	4.65	0.20	15.98	0.030	
	100	8.61	0.18	10.06	0.081	poor fit
	170	17.72	0.29	17.34	0.28	6.52	0.023	
890	60	<0.04	...	-0.04	0.06	17.38	0.033	
	100	<0.03	...	0.08	0.06	9.84	0.027	
	170	0.12	0.04	0.10	0.05	5.98	0.039	
912	60	0.83	0.04	1.03	0.09	14.39	0.045	
	100	2.34	0.28	2.50	0.08	7.93	0.060	
	170	2.82	0.10	2.78	0.12	5.17	0.032	
971	60	0.29	0.02	0.17	0.12	16.75	0.023	
	100	0.83	0.04	0.97	0.10	9.57	0.033	
	170	1.38	0.09	1.31	0.19	6.07	0.040	
984	60	<0.04	...	-0.16	0.13	15.04	0.027	
	100	<0.04	...	0.09	0.10	8.93	0.025	
	170	<0.17	...	-0.07	0.09	5.06	0.020	
1001	60	not observed
	100	<0.02	...	-0.03	0.03	8.28	0.066	
	170	0.23	0.03	0.25	0.05	4.99	0.027	
1002	60	0.94	0.05	0.88	0.10	17.34	0.021	
	100	3.36	0.20	3.37	0.09	8.53	0.050	
	170	5.30	0.11	5.35	0.16	6.53	0.050	
1003	60	0.87	0.04	0.75	0.30	17.59	0.033	
	100	3.94	0.32	3.16	0.23	11.22	0.040	
	170	3.12	0.06	2.50	0.12	4.88	0.013	
1043	60	2.36	0.07	2.61	0.64	16.75	0.015	
	100	7.67	0.35	7.08	0.52	10.77	0.046	
	170	16.72	0.59	13.04	0.78	5.53	0.027	
1047	60	<0.04	...	-0.15	0.12	13.85	0.050	
	100	<0.04	...	-0.20	0.11	8.41	0.032	
	170	<0.21	...	-0.11	0.12	4.12	0.063	
1110	60	1.79	0.24	1.43	0.18	13.89	0.029	
	100	4.08	0.27	4.23	0.32	9.29	0.028	
	170	10.01	0.17	9.41	0.23	6.86	0.038	
1121	60	not observed
	100	<0.02	...	0.04	0.04	9.42	0.035	
	170	-0.12	0.07	4.90	0.012	confusion limited
1158	60	<0.04	...	0.59	0.21	12.13	0.025	
	100	<0.05	...	0.09	0.20	7.32	0.048	
	170	<0.14	...	-0.11	0.11	4.86	0.009	

Table 7—Continued

VCC	λ μm	F_{model}^1 Jy	$\epsilon(F_{\text{model}})$ Jy	F_{map}^2 Jy	$\epsilon(F_{\text{map}})$ Jy	B_{backgr}^3 $\frac{\text{MJy}}{\text{sr}}$	f_B^4	notes
1189	60	0.18	0.02	0.31	0.07	16.86	0.023	
	100	0.49	0.02	0.43	0.07	9.29	0.022	
	170	1.16	0.03	1.15	0.27	5.60	0.033	
1196	60	<0.04	...	-0.14	0.11	12.10	0.043	
	100	<0.04	...	0.07	0.10	8.30	0.049	
	170	1.24	0.32	6.92	0.025	poor fit
1217	60	<0.04	...	-0.20	0.11	14.62	0.019	
	100	<0.03	...	0.10	0.10	9.14	0.033	
	170	<0.07	...	0.08	0.09	5.35	0.021	
1253	60	0.14	0.04	0.16	0.14	12.30	0.043	
	100	0.81	0.09	0.80	0.15	7.16	0.060	
	170	1.13	0.09	1.01	0.11	5.14	0.068	
1326	60	2.36	0.19	2.52	0.06	14.33	0.051	
	100	2.89	0.14	2.48	0.09	9.22	0.065	
	170	2.98	0.31	1.93	0.21	8.60	0.030	
1368	60	<0.15	...	0.02	0.07	16.07	0.034	
	100	<0.03	...	0.03	0.07	10.07	0.040	
	170	0.20	0.05	0.29	0.25	8.47	0.060	
1379	60	1.14	0.06	1.16	0.11	12.12	0.049	
	100	3.27	0.19	3.32	0.11	6.33	0.067	
	170	4.98	0.15	4.65	0.21	6.66	0.023	
1410	60	0.22	0.02	0.39	0.10	13.31	0.040	
	100	0.36	0.03	0.44	0.09	7.50	0.028	
	170	0.69	0.04	0.67	0.12	6.42	0.032	
1412	60	<0.06	...	0.03	0.26	15.98	0.032	
	100	<0.07	...	0.08	0.19	10.36	0.023	
	170	0.71	0.08	0.63	0.32	9.66	0.038	off-center emission
1419	60	0.06	0.02	0.04	0.15	11.60	0.031	
	100	0.28	0.04	0.18	0.07	7.23	0.044	
	170	0.44	0.07	0.17	0.19	5.51	0.046	
1450	60	0.74	0.05	0.75	0.08	10.05	0.048	
	100	2.99	0.23	2.93	0.13	6.59	0.060	
	170	3.96	0.13	3.95	0.18	7.18	0.057	
1552	60	0.29	0.08	0.38	0.14	11.53	0.027	
	100	1.08	0.06	1.19	0.13	7.23	0.054	
	170	1.94	0.13	1.67	0.23	6.33	0.035	
1554	60	5.56	0.25	5.11	0.26	17.06	0.068	
	100	9.07	0.36	8.20	0.22	10.71	0.092	
	170	10.65	0.19	10.21	0.46	7.14	0.013	
1569	60	<0.05	...	0.28	0.11	10.94	0.032	
	100	<0.05	...	0.19	0.11	7.81	0.032	
	170	<0.06	...	0.05	0.05	5.40	0.023	
1575	60	1.11	0.05	1.36	0.07	15.50	0.040	
	100	2.08	0.27	2.05	0.12	8.16	0.074	
	170	2.74	0.14	2.52	0.19	6.35	0.027	
1581	60	<0.03	...	-0.04	0.05	16.94	0.028	
	100	<0.03	...	0.01	0.04	9.68	0.064	
	170	0.33	0.06	0.31	0.11	6.44	0.038	
1673/1676	60	11.32	0.19	17.99	0.030	interacting system
	100	29.34	0.46	12.82	0.095	
	170	96.85	1.56	85.21	0.78	8.21	0.075	

Table 7—Continued

VCC	λ μm	F_{model}^1 Jy	$\epsilon(F_{\text{model}})$ Jy	F_{map}^2 Jy	$\epsilon(F_{\text{map}})$ Jy	B_{backgr}^3 $\frac{\text{MJy}}{\text{sr}}$	f_B^4	notes
1675	60	0.05	0.01	0.09	0.06	15.84	0.019	
	100	<0.03	...	0.03	0.07	9.15	0.028	
	170	0.16	0.04	0.30	0.07	6.39	0.054	
1678	60	0.08	0.01	0.73	0.16	16.67	0.039	
	100	0.43	0.05	0.48	0.15	9.20	0.052	
	170	0.68	0.12	0.66	0.12	7.10	0.048	
1686	60	0.45	0.08	0.32	0.17	12.28	0.025	
	100	1.13	0.06	1.50	0.15	7.90	0.032	
	170	1.49	0.10	1.47	0.23	7.29	0.052	
1690	60	6.20	0.41	7.12	0.46	14.16	0.063	
	100	16.00	0.67	20.05	0.73	8.90	0.032	
	170	29.16	0.32	28.62	0.53	8.35	0.072	
1699	60	0.27	0.04	0.77	0.13	16.61	0.045	
	100	0.39	0.02	0.98	0.12	9.30	0.058	
	170	0.49	0.03	0.49	0.28	7.12	0.035	
1725	60	0.05	0.01	-0.05	0.06	16.03	0.023	
	100	0.30	0.05	0.45	0.08	8.80	0.032	
	170	0.48	0.03	0.45	0.19	6.08	0.092	
1726	60	<0.05	...	0.33	0.07	16.47	0.035	
	100	<0.05	...	0.14	0.08	9.76	0.068	
	170	0.24	0.03	0.49	0.27	6.62	0.041	
1727	60	4.16	0.22	3.91	0.33	16.90	0.026	
	100	12.34	0.41	10.90	0.36	11.87	0.069	
	170	29.19	1.20	22.91	0.35	9.38	0.055	
1730	60	1.52	0.22	2.22	0.15	15.20	0.042	
	100	3.64	0.26	4.41	0.12	6.86	0.078	
	170	5.46	0.55	5.32	0.12	7.84	0.049	
1750	60	<0.03	...	0.22	0.05	15.45	0.044	
	100	0.04	0.01	0.28	0.05	8.90	0.070	
	170	0.08	0.02	0.11	0.04	6.02	0.043	
1757	60	0.10	0.01	-0.42	0.09	14.04	0.023	
	100	0.50	0.02	1.02	0.10	8.32	0.042	
	170	0.79	0.03	0.79	0.12	6.47	0.064	

¹The flux F_{model} derived from integrating the model fit to infinity. The upper limits are indicated with a ‘<’ sign in front;

²The flux F_{map} derived from integrating the raw maps;

³The average background brightness B_{backgr} ;

⁴The 1σ fractional uncertainty f_B in the background brightness, determined from the spread in the response of individual detector pixels to the background at the ends of the scans.